The APOGEE value-added catalogue of Galactic globular cluster stars

Ricardo P. Schiavon [1]★ Siân G. Phillips [1]★ Natalie Myers,[2] Danny Horta [1,3]★ Dante Minniti,[4,5,6]
Carlos Allende Prieto,[7,8] Borja Anguiano,[9,10] Rachael L. Beaton,[11,12] Timothy C. Beers,[13] Joel
R. Brownstein [14] Roger E. Cohen,[15] José G. Fernández-Trincado [16] Peter M. Frinchaboy,[2]
Henrik Jönsson,[17] Shobhit Kisku,[1] Richard R. Lane,[18] Steven R. Majewski,[10] Andrew C. Mason,[1]
Szabolcs Mészáros[19,20] and Guy S. Stringfellow [21]

Affiliations are listed at the end of the paper

ABSTRACT

We introduce the Sloan Digital Sky Survey (SDSS)/ Apache Point Observatory Galactic Evolution Experiment (APOGEE) value-added catalogue of Galactic globular cluster (GC) stars. The catalogue is the result of a critical search of the APOGEE Data Release 17 (DR17) catalogue for candidate members of all known Galactic GCs. Candidate members are assigned to various GCs on the basis of position in the sky, proper motion, and radial velocity. The catalogue contains a total of 7737 entries for 6422 unique stars associated with 72 Galactic GCs. Full APOGEE DR17 information is provided, including radial velocities and abundances for up to 20 elements. Membership probabilities estimated on the basis of precision radial velocities are made available. Comparisons with chemical compositions derived from the GALactic Archaeology with HERMES (GALAH) survey, as well as optical values from the literature, show good agreement. This catalogue represents a significant increase in the public data base of GC star chemical compositions and kinematics, providing a massive homogeneous data set that will enable a variety of studies. The catalogue in FITS format is available for public download from the SDSS-IV DR17 value-added catalogue website.

Key words: catalogues – stars: abundances – Galaxy: abundances – globular clusters: general.

1 INTRODUCTION

Globular clusters (GCs) are intriguing objects. The physics of their genesis is not entirely understood, yet their study has advanced knowledge in several fields of astrophysics. The mapping of the spatial distribution of Galactic GCs promoted a radical revision of the position of the Solar system in the Universe (Shapley 1918); application of the physics of stellar structure and evolution to GC observations constrained the age of the Universe in the early days of big bang cosmology (e.g. Sandage 1970; Bolte & Hogan 1995, and references therein); GC ages, chemical compositions, and orbital properties provide important clues to the star formation and accretion history of the early Milky Way (e.g. Searle & Zinn 1978; Salaris & Weiss 2002; Kruijssen et al. 2019; Massari, Koppelman & Helmi 2019; Forbes 2020; Horta et al. 2020; Callingham et al. 2022) and other galaxies (Brodie & Strader 2006, and references therein); finally and no less crucially, to this day GCs are fundamental test beds of stellar evolution theory in the low-mass regime (e.g. Schwarzschild 1970; Renzini & Fusi Pecci 1988; Chiosi, Bertelli & Bressan 1992; Salaris, Cassisi & Weiss 2002). Yet after over a century of study, their origin is still subject to debate, with no shortage of formation scenarios (e.g. Fall & Rees 1985; Schweizer 1987; Ashman & Zepf

1992) despite recent encouraging progress (e.g. Kruijssen 2015; Choksi, Gnedin & Li 2018; Pfeffer et al. 2018).

Since GCs stand at the crossroads of many areas of astrophysics, it is small wonder that they have been subject to various herculean observational efforts over the past several decades – in fact, so many that an exhaustive account is rendered impossible in this brief introduction. We thus limit ourselves to mentioning a few highlights and some of the most recent work, in a manner dictated by the authors' own personal biases and an unavoidably limited grasp of an overwhelming – and ever-growing – literature.

Systematic photometric observations built ground- and space-based colour–magnitude diagrams of large GC samples in the optical (e.g. Barbuy, Bica & Ortolani 1998; Rosenberg et al. 2000; Piotto et al. 2002; Sarajedini et al. 2007; Stetson et al. 2019), near-infrared (NIR; e.g. Cohen et al. 2017; Minniti et al. 2017), and ultraviolet (e.g. Schiavon et al. 2012; Sahu et al. 2022). Libraries of integrated spectra were created for comparison against observations of extragalactic GCs and reality checking of stellar population synthesis models (e.g. Zinn & West 1984; Bica & Alloin 1986; Armandroff & Zinn 1988; Puzia et al. 2002; Schiavon et al. 2005), and more recently integral field spectroscopy of large GC samples have also become available (e.g. Usher et al. 2017; Kamann et al. 2018). In this context, the GC system of the Andromeda galaxy has also become subject to extensive integrated light surveys both in optical and NIR (e.g. Galleti et al. 2007; Caldwell et al. 2009; Schiavon et al. 2013; Sakari et al. 2016). Finally, with the advent of the *Gaia* satellite, a massive undertaking by E. Vasiliev and H. Baumgardt has produced precision kinematics

★ E-mail: r.p.schiavon@ljmu.ac.uk (RPS); S.G.Phillips@ljmu.ac.uk (SGP); dhortadarrington@flatironinstitute.org (DH)

and structural parameters for the vast majority of known Galactic GCs (Baumgardt & Vasiliev 2021; Vasiliev & Baumgardt 2021).

Chemical compositions of individual GC stars constitute precious, and quite expensive, information for a variety of scientific pursuits. Within the confines of stellar evolution theory, such pursuits include the calibration of evolutionary tracks, the study of stellar evolution processes such as dredge-up and deep mixing along the giant branch (e.g. Kraft 1979; Shetrone 1996), and diffusion of heavy elements in main-sequence stars (e.g. Denissenkov & Weiss 1996; Castellani & degl'Innocenti 1999; Lind et al. 2008). The first systematic collection of chemical compositions of individual stars in Galactic GCs was conducted by the Lick/Texas group (e.g. Kraft 1994; Shetrone 1996; Sneden et al. 1997). Contrary to the generally agreed notion of GCs as coeval stellar systems with homogeneous chemical compositions, these early efforts revealed that star-to-star abundance variations are ubiquitous. These were difficult to understand, but since the data were restricted to bright giant stars, the broad consensus was that such variations should be ascribed to stellar evolution effects.

The next generation of systematic measurements brought about a considerable amplification of the existing data base of homogeneously derived chemical compositions (e.g. Carretta & Gratton 1997; Carretta et al. 2010, and references therein). These efforts consolidated the knowledge that star-to-star chemical composition variations are the norm in GCs. They typically manifest themselves in the form of anticorrelations between the abundances of light elements such as C–N, Na–O, and Mg–Al (e.g. Gratton, Carretta & Bragaglia 2012). Such abundance variations are present in main-sequence stars (e.g. Cannon et al. 1998), ruling out evolutionary effects as their physical origin. In addition to these features, massive systems such as ω Cen,[1] among others, display variations in the abundances of the heavy elements that are by-products of Type Ia supernova (SN Ia) enrichment (e.g. Pancino et al. 2002; Johnson & Pilachowski 2010).

The discovery of multiple sequences in colour–magnitude diagrams, made possible by the significant increase in photometric precision afforded by the *Hubble Space Telescope* (*HST*)/Advanced Camera for Surveys (ACS), prompted the conclusion that GCs host a complex mix of stellar populations. In view of this overwhelming evidence, the historical assumption that GCs are single stellar populations had to be dropped. This so-called *multiple populations (MPs) phenomenon* is without a doubt inextricably linked to the physics of GC formation. Yet no formation scenarios are capable of accounting for this phenomenon in a quantitative fashion (see reviews by Renzini et al. 2015; Bastian & Lardo 2018; Milone & Marino 2022).

A solution to the problem of MPs in GCs, and in a broader perspective our understanding of the nature of these beautiful and fascinating systems, can be advanced by the production of a massive, homogeneous, and publicly available data base of chemical compositions and kinematics for a large sample of Galactic GCs. This paper summarizes the effort by the Apache Point Observatory Galactic Evolution Experiment (APOGEE) team to make one such data base available for public access. We present the APOGEE value-added catalogue (VAC) of Galactic GC members. This paper is organized as follows. In Section 2, we briefly describe the APOGEE data. In Section 3, the criteria adopted for selecting candidate GC members

are described, while membership probabilities are discussed in Section 4. Broad features of the data are presented in Section 5, and Section 6 describes the catalogue and provides access information.

2 THE DATA

This paper presents a catalogue of chemical compositions and radial velocities (RVs) from the latest data release of the Sloan Digital Sky Survey IV (SDSS-IV)/APOGEE-2 survey (Data Release 17 – DR17; Majewski et al. 2017; Abdurro'uf et al. 2022). Proper motions (PMs) from the Early Data Release 3 (EDR3) from the *Gaia* satellite (Gaia Collaboration 2021) and various additional metadata imported directly from the DR17 catalogue are also included for convenience's sake. Data from APOGEE have been described in detail in various technical publications, so we provide a brief account of their main properties in this section, referring the reader to the relevant papers for further details. Chemical composition data based on earlier APOGEE data releases were presented for various collections of Galactic GCs in a number of publications (e.g. Mészáros et al. 2015, 2020, 2021; Schiavon et al. 2017b; Masseron et al. 2019; Nataf et al. 2019; Geisler et al. 2021).

Elemental abundances and RVs are obtained from the automatic analysis of moderately high-resolution NIR spectra of hundreds of thousands of stars observed with the Apache Point Observatory 2.5-m Sloan telescope (Gunn et al. 2006) and the Las Campanas Observatory 2.5-m Du Pont telescope (Bowen & Vaughan 1973). The telescopes are equipped with twin high-efficiency multifibre NIR spectrographs designed and assembled at the University of Virginia, USA (Wilson et al. 2019). A technical summary of the overall SDSS-IV experiment can be found in Blanton et al. (2017).

APOGEE spectra for any given star (save for a relatively small number of exceptions) were obtained in a number of visits separated in time to enable the detection of RV variations caused by binarity. Observations spanned a period of typically 3 months, never exceeding 6 months between the first and last visit. Every visit spectrum was integrated typically for ∼1 h in sets of four (ABBA) exposures taken with the detector dithered along the spectral direction. Spectral dithers were aimed at bringing the sampling of the line spread function to slightly better than critical in the blue end of the spectrum where the sampling by the detector's original pixel size is subcritical.

A pipeline built specifically for the reduction of APOGEE data (Nidever et al. 2015) was employed to apply standard operations such as reference pixel voltage correction, linearization, cosmic ray and saturation corrections, dark current subtraction, persistence correction, and extraction of the 2D data array from the 3D data cubes. The 2D images were then flat-field corrected and a bad-pixel mask was generated before 1D spectra were extracted, and subsequently wavelength and flux calibrated. The next step was to subtract the sky background, which is dominated by emission lines, and perform telluric correction before combining the dithered sequences into a single well-sampled resulting visit spectrum.

For each star, relative RVs of visit spectra were measured through iterative cross-correlation with the combined spectrum, and final absolute RVs were then obtained by cross-correlation of the combined spectrum with a grid of synthetic spectra covering a wide range of stellar parameters. The resulting combined rest-frame spectrum is that which is finally fed into the stellar abundances pipeline.

The APOGEE Stellar Parameters and Chemical Abundances Pipeline (ASPCAP) is described in detail by García Pérez et al. (2016) and later updates by Holtzman et al. (2018) and Jönsson et al. (2020). In short, it determines stellar parameters and detailed elemental abun-

---

[1]It bears mentioning at this point that ω Cen is now believed to be the remnant nuclear cluster of a dwarf galaxy long accreted to the Milky Way (e.g. Bekki & Freeman 2003; Majewski et al. 2012), which more recently has been potentially identified (e.g. Massari et al. 2019; Pfeffer et al. 2021) as Gaia Enceladus/Sausage (Belokurov et al. 2018; Helmi et al. 2018) or Sequoia (Myeong et al. 2019; Forbes 2020).

dances through interpolation, using the FERRE[2] software (Allende Prieto et al. 2006), into a huge grid of synthetic spectra covering the entire range of stellar parameters and chemical compositions of interest. The spectral library is calculated adopting MARCS model atmospheres (Gustafsson et al. 2008) generated specifically for the purposes of the APOGEE survey (see Mészáros et al. 2012; Zamora et al. 2015; Holtzman et al. 2018; Jönsson et al. 2018). ASPCAP abundance analysis is based on various flavours of line lists, depending on the spectrum synthesis codes, local thermodynamic equilibrium (LTE)/non-local thermodynamic equilibrium (NLTE) assumption, and model atmospheres adopted in the construction of the spectral library. Those line lists are empirically tuned to match the observed high-resolution spectra of the Sun and Arcturus. For details, see Smith et al. (2021) (but also see Shetrone et al. 2015; Hasselquist et al. 2016; Cunha et al. 2017).

The data described above were made publicly available in DR17 in the form of various catalogues for different flavours of spectral analysis, according to the spectrum synthesis code adopted in the construction of the spectral library, adoption or not of an NLTE approach for some elements,[3] and the assumption of plane-parallel or spherical geometry in the radiative transfer calculation. Each catalogue contains 733 901 entries. The data contained in this VAC are extracted from the default DR17 data analysis, which is based on the SYNSPEC-based (Hubeny & Lanz 2017) spectral library, with incorporation of an NLTE abundance analysis for elements Na, Mg, K, and Ca (prefix synspec_rev1; see Osorio et al. 2020, and references therein).

2.1 Globular cluster sample

Globular clusters (GCs) were targeted by APOGEE so as to satisfy at the same time scientific interests and calibration needs. As the first attempt at automatic detailed chemical composition analysis of a massive NIR spectroscopic data base, optical calibrators are a crucial requirement for APOGEE. As targets of interest for various scientific pursuits, GC stars have for decades been the focus of chemical composition studies. Thus the availability of multiple elemental abundance determinations in the literature, overwhelmingly based on optical spectroscopy, placed GC stars at the centre of the APOGEE calibration procedure (e.g. Holtzman et al. 2015, 2018; Jönsson et al. 2020). With those goals in mind, a large number of GCs were targeted during the execution of both APOGEE-1 and APOGEE-2. Targets within each GC were selected to meet a set of criteria whereby stars that were subject to previous abundance analysis and/or atmospheric parameter determinations were given top priority, followed by stars with membership confirmed on the basis of RV, PM, and position on the colour–magnitude diagram, in decreasing order of priority (for details, see Zasowski et al. 2013, 2017; Beaton et al. 2021; Santana et al. 2021). In addition to the GCs targeted as part of the main APOGEE survey, a number of additional systems were observed as part of the bulge Cluster APOgee Survey (CAPOS; Geisler et al. 2021). The CAPOS team took advantage of Chilean access to the APOGEE-South spectrograph (Wilson et al. 2019) to collect data for a number of GCs located towards the inner Galaxy. CAPOS spectra were collected, reduced, and analysed following the same procedures and pipelines as the main survey targets, with results being ingested into the SDSS/APOGEE data base. Data obtained by CAPOS are thus treated in this paper in the same way as the targets from the main APOGEE survey. Table 1 lists the GCs included in this VAC, along with basic parameters, extracted from Baumgardt & Vasiliev (2021) and Vasiliev & Baumgardt (2021),[4] which we hereafter refer simply as the VB catalogue. The number of candidate members of each GC is also listed. The distribution of our GC sample in Cartesian coordinates is shown in Fig. 1. Unfortunately, GCs whose discovery was reported after the latest update of the VB catalogue, such as VVV CL001 (Fernández-Trincado et al. 2021b) and Patchick 125 (Fernández-Trincado et al. 2022), are not included in this catalogue, but will be incorporated in future versions.

3 SELECTING CLUSTER MEMBER CANDIDATES

The number of stars targeted per GC varied widely as a function of the number of visits, apparent magnitude, and apparent GC size, which constrains the number of possible targets in any given visit by virtue of the fibre collision radius of ∼1 arcmin. Moreover, the fraction of bona fide GC members from previous studies also vary widely across the GC sample, as does the number of targets lacking a previous membership assignment based on RV or PM measurement.

The situation mandates a strategy based on a sweeping search of the entire APOGEE DR17 catalogue for GC members defined according to a set of homogeneous membership criteria. By proceeding in this way we hope to generate a catalogue that confirms previously established memberships while further extending member samples on the basis of good-quality RVs and PMs.

The philosophy underlying our approach is to generously consider every star with a reasonable probability of belonging to a given GC, providing elements to enable the catalogue users to make their own informed sample selections. In short, catalogue completeness is prioritized over purity. Nevertheless, the catalogue is devised in such a way as to make a conservative selection leading up to a very pure sample quite straightforward.

Stars are selected on the basis of angular distance from GC centre, PM, and RV only. Criteria for selection are defined in terms of the GC's Jacobi radius (r_J), as well as central values and dispersion of PMs (μ_{PM} and σ_{PM}) and RVs (μ_{RV} and σ_{RV}). We decided not to use position in the colour–magnitude diagram as a selection criterion, to avoid biasing against possible minority populations. We adopt the following sets of criteria to define two broad types of candidate members.

(i) *Likely members* are those meeting a *strict* set of angular distance, PM, and RV criteria, *regardless of their chemical compositions*.

(ii) *Outliers* are stars meeting more relaxed angular distance, PM, and RV criteria, whose metallicities match closely those of nearby GCs.

The *Likely* group, as its name indicates, contains the stars that have the highest probability of being cluster members. By not imposing a metallicity condition to define this group we wish to avoid missing members for which ASPCAP could not find a metallicity solution (the case of very warm stars) or those with potentially large errors in metallicity [the case of both very warm and very cool stars or those with low signal-to-noise ratio (S/N) spectra]. Moreover, *Likely* members with very discrepant metallicities could represent a fringe GC population. Conversely, the *Outlier* group contains stars whose chemical compositions are consistent with membership, but whose posi-

---

[2]Available at https://github.com/callendeprieto/ferre
[3]For details see https://www.sdss.org/dr17/irspec/spectro_data_supplement

[4]Available at https://people.smp.uq.edu.au/HolgerBaumgardt/globular/

Table 1. Globular clusters (GCs) included in the sample. Column information: (1) GC ID; (2) and (3) coordinates of GC centre; (4) mean iron abundance; (5) mean radial velocity (RV); (6) heliocentric distance; (7) Galactocentric distance; (8) mass; (9) Jacobi radius; and (10) number of entries. Numbers for columns (2), (3), (5), (6), (7), (8), and (9) are from the VB catalogue, whereas those for columns (4) and (10) are from this work.

GC	α_{cen} (°)	δ_{cen} (°)	$\langle \lceil Fe/H \rceil \rangle$	$\langle RV \rangle$ (km s^{-1})	$d_\odot$ (kpc)	R_{GC} (kpc)	Mass (10^4 M$_\odot$)	r_J (°)	N
(1)	(2)	(3)	(4)	(5)	(6)	(7)	(8)	(9)	(10)
NGC 104	6.02379	−72.08131	−0.74	−17.45 ± 0.16	4.52 ± 0.03	7.52 ± 0.01	89.5 ± 0.6	1.557	297
NGC 288	13.18850	−26.58261	−1.27	−44.45 ± 0.13	8.99 ± 0.09	12.21 ± 0.06	9.3 ± 0.3	0.605	43
NGC 362	15.80942	−70.84878	−1.11	223.12 ± 0.28	8.83 ± 0.10	9.62 ± 0.06	28.4 ± 0.4	0.598	70
Palomar 1	53.33350	79.58105	−0.45	−75.72 ± 0.29	11.28 ± 0.32	17.41 ± 0.29	0.10 ± 0.02	0.122	3
NGC 1851	78.52816	−40.04655	−1.13	321.4 ± 1.55	11.95 ± 0.13	16.69 ± 0.11	31.8 ± 0.4	0.611	71
NGC 1904	81.04584	−24.52442	−1.52	205.76 ± 0.2	13.08 ± 0.18	19.09 ± 0.16	13.9 ± 1.0	0.259	40
NGC 2298	102.24754	−36.00531	−1.84	147.15 ± 0.57	9.83 ± 0.17	15.07 ± 0.14	5.6 ± 0.8	0.435	12
NGC 2808	138.01291	−64.86349	−1.07	103.57 ± 0.27	10.06 ± 0.11	11.58 ± 0.07	86.4 ± 0.6	0.944	132
NGC 3201	154.40343	−46.41248	−1.39	493.65 ± 0.21	4.74 ± 0.04	8.93 ± 0.02	16.0 ± 0.3	0.925	217
NGC 4147	182.52626	18.54264	−1.63	179.35 ± 0.31	18.53 ± 0.21	20.2 ± 0.2	3.9 ± 0.9	0.274	3
Rup 106	189.66750	−51.15028	−1.30	−38.36 ± 0.26	20.71 ± 0.36	18.0 ± 0.3	3.4 ± 0.6	0.213	2
NGC 4590	189.86658	−26.74406	−2.22	−93.11 ± 0.18	10.40 ± 0.10	10.35 ± 0.07	12.2 ± 0.9	0.426	41
NGC 5024	198.23021	18.16817	−1.90	−63.37 ± 0.25	18.50 ± 0.18	19.0 ± 0.16	45.5 ± 3.0	0.549	41
NGC 5053	199.11288	17.70025	−2.21	42.82 ± 0.25	17.54 ± 0.23	18.01 ± 0.2	7.4 ± 2.0	0.317	17
NGC 5139	201.69699	−47.47947	−1.60	232.78 ± 0.21	5.43 ± 0.05	6.5 ± 0.01	364 ± 4	2.142	1864
NGC 5272	205.54842	28.37728	−1.43	−147.2 ± 0.27	10.17 ± 0.08	12.09 ± 0.06	41.0 ± 1.7	0.714	299
NGC 5466	211.36371	28.53444	−1.81	106.82 ± 0.2	16.12 ± 0.16	16.47 ± 0.13	6.0 ± 1.0	0.284	17
NGC 5634	217.40533	−5.97643	−1.72	−16.07 ± 0.6	25.96 ± 0.62	21.84 ± 0.57	22.8 ± 4.0	0.42	2
Palomar 5	229.01917	−0.121	−1.24	−58.61 ± 0.15	21.94 ± 0.51	17.27 ± 0.47	1.0 ± 0.2	0.12	12
NGC 5904	229.63841	2.08103	−1.21	53.5 ± 0.25	7.48 ± 0.06	6.27 ± 0.02	39.4 ± 0.6	0.607	259
NGC 6093	244.26004	−22.97608	−1.61	10.93 ± 0.39	10.34 ± 0.12	3.95 ± 0.08	33.8 ± 0.9	0.344	3
NGC 6121	245.86974	−26.52575	−1.07	71.21 ± 0.15	1.85 ± 0.02	6.45 ± 0.01	8.7 ± 0.1	1.658	224
NGC 6144	246.80777	−26.0235	−1.80	194.79 ± 0.58	8.15 ± 0.13	2.5 ± 0.02	7.9 ± 1.4	0.198	1
NGC 6171	248.13275	−13.05378	−1.02	−34.71 ± 0.18	5.63 ± 0.08	3.74 ± 0.04	7.5 ± 0.4	0.368	65
NGC 6205	250.42181	36.45986	−1.48	−244.9 ± 0.3	7.42 ± 0.08	8.64 ± 0.04	54.5 ± 2.0	1.036	152
NGC 6229	251.74525	47.5278	−1.24	−137.89 ± 0.71	30.11 ± 0.47	29.45 ± 0.44	28.6 ± 9.0	0.395	11
NGC 6218	251.80907	−1.94853	−1.27	−41.67 ± 0.14	5.11 ± 0.05	4.57 ± 0.02	10.7 ± 0.3	0.508	107
NGC 6254	254.28772	−4.10031	−1.51	74.21 ± 0.23	5.07 ± 0.06	4.35 ± 0.03	20.5 ± 0.4	0.611	87
NGC 6273	255.65749	−26.26797	−1.71	145.54 ± 0.59	8.34 ± 0.16	1.43 ± 0.03	69.7 ± 3.6	0.266	81
NGC 6293	257.54250	−26.58208	−2.09	−143.66 ± 0.39	9.19 ± 0.28	1.6 ± 0.18	20.5 ± 1.6	0.153	20
NGC 6304	258.63440	−29.46203	−0.48	−108.62 ± 0.39	6.15 ± 0.15	2.19 ± 0.13	12.6 ± 1.1	0.276	34
NGC 6316	259.15542	−28.14011	−0.77	99.65 ± 0.84	11.15 ± 0.39	3.16 ± 0.36	32.8 ± 4.0	0.271	24
NGC 6341	259.28076	43.13594	−2.25	−120.55 ± 0.27	8.50 ± 0.07	9.84 ± 0.04	35.2 ± 0.4	0.808	80
Terzan 2	261.88792	−30.80233	−0.86	134.56 ± 0.96	7.75 ± 0.33	0.74 ± 0.16	13.6 ± 2.5	0.084	5
Terzan 4	262.66251	−31.59553	−1.38	−48.96 ± 1.57	7.59 ± 0.31	0.82 ± 0.2	20.0 ± 5.0	0.125	3
HP 1	262.77167	−29.98167	−1.21	39.76 ± 1.22	6.99 ± 0.14	1.26 ± 0.13	12.4 ± 1.7	0.156	17
FSR 1758	262.8	−39.808	−1.42	227.31 ± 0.59	11.08 ± 0.74	3.46 ± 0.63	62.8 ± 5.6	0.618	15
Liller 1	263.35233	−33.38956	−0.14	60.36 ± 2.44	8.06 ± 0.35	0.74 ± 0.07	91.5 ± 14.7	0.261	30
NGC 6380	263.61861	−39.06953	−0.78	−1.48 ± 0.73	9.61 ± 0.30	2.15 ± 0.21	33.4 ± 0.5	0.233	28
Ton 2	264.03929	−38.54092	−0.74	−184.72 ± 1.12	6.99 ± 0.33	1.76 ± 0.19	6.9 ± 1.6	0.166	11
NGC 6388	264.07178	−44.7355	−0.49	83.11 ± 0.45	11.17 ± 0.16	3.99 ± 0.13	125.0 ± 1.0	0.516	75
NGC 6401	264.65219	−23.9096	−1.09	−105.44 ± 2.5	8.06 ± 0.24	0.75 ± 0.04	14.5 ± 0.2	0.094	7
NGC 6397	265.17538	−53.67434	−2.02	18.51 ± 0.08	2.48 ± 0.02	6.01 ± 0.02	9.7 ± 0.1	1.174	187
Palomar 6	265.92581	−26.22499	−0.92	177.0 ± 1.35	7.05 ± 0.45	1.33 ± 0.45	9.5 ± 1.7	0.124	6
Terzan 5	267.02020	−24.77906	−0.78	−82.57 ± 0.73	6.62 ± 0.15	1.65 ± 0.13	93.5 ± 6.9	0.422	24
NGC 6441	267.55441	−37.05145	−0.49	18.47 ± 0.56	12.73 ± 0.16	4.78 ± 0.15	132.0 ± 1.0	0.502	25
UKS1	268.61331	−24.14528	−1.00	59.38 ± 2.63	15.58 ± 0.56	7.7 ± 0.5	7.7 ± 0.	0.17	5
Terzan 9	270.41167	−26.83972	−1.36	68.49 ± 0.56	5.77 ± 0.34	2.46 ± 0.32	12.0 ± 1.4	0.295	23
Djorg 2	270.45438	−27.82582	−1.07	−149.75 ± 1.1	8.76 ± 0.18	0.8 ± 0.13	12.5 ± 0.3	0.079	10
NGC 6517	270.46075	−8.95878	−1.58	−35.06 ± 1.65	9.23 ± 0.56	3.24 ± 0.26	19.5 ± 2.8	0.27	1
Terzan 10	270.74083	−26.06694	−1.62	211.37 ± 2.27	10.21 ± 0.40	2.17 ± 0.37	30.2 ± 5.6	0.191	2
NGC 6522	270.89198	−30.03397	−1.22	−15.23 ± 0.49	7.30 ± 0.21	1.04 ± 0.17	21.1 ± 1.3	0.181	15
NGC 6528	271.2067	−30.05578	−0.16	211.86 ± 0.43	7.83 ± 0.24	0.7 ± 0.1	5.7 ± 0.7	0.067	4
NGC 6539	271.20728	−7.58586	−0.74	35.19 ± 0.5	8.17 ± 0.39	3.09 ± 0.07	20.9 ± 1.7	0.317	1
NGC 6540	271.53566	−27.76529	−1.02	−16.5 ± 0.78	5.91 ± 0.27	2.34 ± 0.25	3.5 ± 1.2	0.165	6
NGC 6544	271.83383	−24.99822	−1.52	−38.46 ± 0.67	2.58 ± 0.06	5.62 ± 0.06	9.1 ± 0.6	1.078	27
NGC 6553	272.31532	−25.90775	−0.19	−0.27 ± 0.34	5.33 ± 0.13	2.83 ± 0.13	28.5 ± 1.6	0.494	17
NGC 6558	272.57397	−31.76451	−0.99	−195.12 ± 0.73	7.47 ± 0.25	0.8 ± 0.17	2.65 ± 0.08	0.073	6
Terzan 12	273.06583	−22.74194	−0.56	95.61 ± 1.21	5.17 ± 0.38	3.17 ± 0.34	8.7 ± 2.0	0.312	6
NGC 6569	273.41167	−31.82689	−0.92	−49.83 ± 0.5	10.53 ± 0.26	2.59 ± 0.23	23.6 ± 2.0	0.226	14
NGC 6642	277.97596	−23.4756	−1.09	−60.61 ± 1.35	8.05 ± 0.20	1.66 ± 0.01	3.4 ± 0.1	0.11	12

Table 1 – *continued*

GC	$\alpha_{\rm cen}$	$\delta_{\rm cen}$	$\langle\lceil{\rm Fe/H}\rceil\rangle$	$\langle{\rm RV}\rangle$	$d_\odot$	$R_{\rm GC}$	Mass	$r_{\rm J}$	N
	(°)	(°)		(km s^{-1})	(kpc)	(kpc)	($10^4\,{\rm M}_\odot$)	(°)	
(1)	(2)	(3)	(4)	(5)	(6)	(7)	(8)	(9)	(10)
NGC 6656	279.09976	−23.90475	−1.70	−148.72 ± 0.78	3.30 ± 0.04	5.0 ± 0.03	47.6 ± 0.5	1.308	412
NGC 6715	283.76385	−30.47986	−0.62	143.13 ± 0.43	26.28 ± 0.33	18.51 ± 0.32	178.0 ± 3.0	0.618	1809
NGC 6717	283.77518	−22.70147	−1.12	30.25 ± 0.9	7.52 ± 0.13	2.38 ± 0.02	3.6 ± 0.8	0.151	5
NGC 6723	284.88812	−36.63225	−1.02	−94.39 ± 0.26	8.27 ± 0.10	2.47 ± 0.02	17.7 ± 1.1	0.258	9
NGC 6752	287.7171	−59.98455	−1.47	−26.01 ± 0.12	4.12 ± 0.04	5.3 ± 0.02	27.6 ± 0.4	0.913	152
NGC 6760	287.80027	1.03047	−0.75	−2.37 ± 1.27	8.41 ± 0.43	5.17 ± 0.14	26.9 ± 2.5	0.488	11
Palomar 10	289.50693	18.57899	0.02	−31.7 ± 0.23	8.94 ± 1.18	7.6 ± 0.59	16.2 ± 2.7	0.431	3
NGC 6809	294.99878	−30.96475	−1.76	174.7 ± 0.17	5.35 ± 0.05	4.01 ± 0.03	19.3 ± 0.8	0.549	98
NGC 6838	298.44373	18.77919	−0.75	−22.72 ± 0.2	4.00 ± 0.05	6.86 ± 0.01	4.6 ± 0.2	0.619	129
NGC 7078	322.49304	12.167	−2.29	−106.84 ± 0.3	10.71 ± 0.10	10.76 ± 0.07	63.3 ± 0.7	0.757	155
NGC 7089	323.36258	−0.82325	−1.47	−3.78 ± 0.3	11.69 ± 0.11	10.54 ± 0.08	62.7 ± 1.1	0.548	36
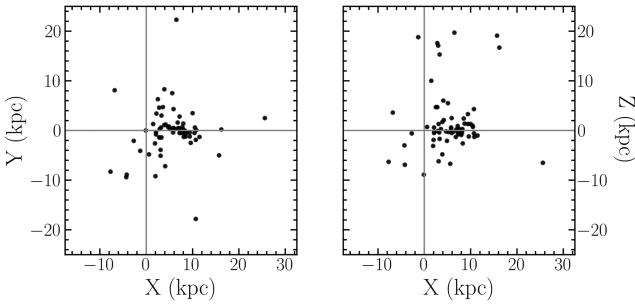
Figure 1. Spatial distribution of the GCs included in this VAC, in Cartesian coordinates with the Sun at the origin (cross-hairs). The sample is preferentially concentrated towards the inner Galaxy.

Table 2. Definition of two subgroups of candidate members. Column information: (1) subgroup type; (2) angular distance limits in units of the Jacobi radius, given in Table 1; (3) proper motion (PM) limits; (4) radial velocity (RV) limits; and (5) $\lceil{\rm Fe/H}\rceil$ limits. Limits in columns (3)–(5) in units of residuals are defined as $\delta X = \frac{{\rm res}(X)}{\sigma_X}$, where ${\rm res}(X) = |X - \mu_X|$, and μ_X and σ_X stand for the mean and rms scatter of each observable, respectively.

Subgroup	Distance	PM	RV	$\lceil{\rm Fe/H}\rceil$
(1)	(2)	(3)	(4)	(5)
Likely	$r < r_{\rm J}$	$\delta\,{\rm PM} < 2$	$\delta\,{\rm RV} < 2$	Any
Outlier	$r_{\rm J} < r < 4r_{\rm J}$ [a]	$2 < \delta\,{\rm PM} < 10$	$2 < \delta\,{\rm RV} < 3$	$\delta\,\lceil{\rm Fe/H}\rceil < 2$

Note. [a]For GCs located in crowded fields towards the inner Galaxy, the initial search radius was reduced from $4r_{\rm J}$ to $2r_{\rm J}$, in order to minimize contamination by field stars.

tion and kinematics suggest at best a loose association. Inclusion of the *Outlier* group aims at catching a maximum number of extra-tidal stars. In cases of GCs presenting a large spread in metallicity, such as ω Cen, M54, Terzan 5, or Liller 1, similarity in terms of [Fe/H] cannot be used to define *Outliers*, although those with abundance patterns consistent with a second-generation nature are retained and flagged.

The quantitative definitions of these two subgroups are provided in Table 2. GC centre coordinates and the values for $r_{\rm J}$, $\mu_{\rm PM}$, $\mu_{\rm RV}$, and $\sigma_{\rm RV}$ were adopted from the VB catalogue. The generous upper angular distance limits adopted for *Outliers* are aimed at enabling the identification of extra-tidal GC members. The method to estimate $\sigma_{\rm PM}$ is described below. The very generous PM threshold was adopted after we found out that some good candidates were located several $\sigma_{\rm PM}$ off of the mean PM value, which may reflect our admittedly rough estimate of $\sigma_{\rm PM}$.

Our procedure can be summarized as follows. We start by obtaining an estimate of the proper motion (PM) dispersion, $\sigma_{\rm PM}$. Data from the *Gaia* EDR3 archive were downloaded for each cluster. Adopting mean PM values from the VB catalogue we calculated $\sigma_{\rm PM}$ through a single σ-clipping iteration aimed at removing background contamination. That measured dispersion is obviously larger than the intrinsic dispersion since it folds in measurement errors that are not the same for every cluster. Given those estimates, stars are considered to be *Likely* GC members if they meet the set of strict criteria listed in the first row of Table 2. Next, the APOGEE catalogue was searched for *Outliers*, by following the set of loose criteria listed in the second row of Table 2. The selection process is illustrated in Fig. 2.

The resulting sample consists of a total of 7737 entries for 6424 unique candidate members associated with 72 GCs. Multiple entries occur for a number of stars located in overlapping fields and/or observed as part of different programs. The quality of the data is illustrated in Fig. 3, which shows the distribution of the median S/N pixel^{-1} of the resulting sample, where ∼93 per cent of the spectra have S/N > 50. The distributions of the stars in the Kiel diagram and *Gaia* colour–magnitude diagram are shown in Fig. 4. The right panel shows the distribution of the sample stars in the *Gaia* undereddened colour–magnitude diagram, where the range of GC metallicities can be immediately appreciated. In the left panel, sample stars are displayed in the Kiel diagram, which brings to sharp relief the high precision of APOGEE stellar parameters.

4 MEMBERSHIP PROBABILITIES

In order to provide users of this catalogue with the elements required for deciding which samples should be considered for their analysis, two sets of membership probabilities are provided. The first set is based on a Gaussian mixture modelling of the *Gaia* EDR3 positions and PMs of GC stars, and directly imported from the VB catalogue (Section 4.1). In addition, we derive our own set of independent membership probabilities, based on the APOGEE RVs.

4.1 Vasiliev & Baumgardt probabilities

For the user's convenience we briefly summarize the membership probability estimates provided in the VB catalogue. For further details, the user is referred to the original papers (Baumgardt & Vasiliev 2021; Vasiliev & Baumgardt 2021). Membership probabilities were determined via a mixture modelling approach from which they also inferred cluster properties such as mean parallax, PM, dispersion, and
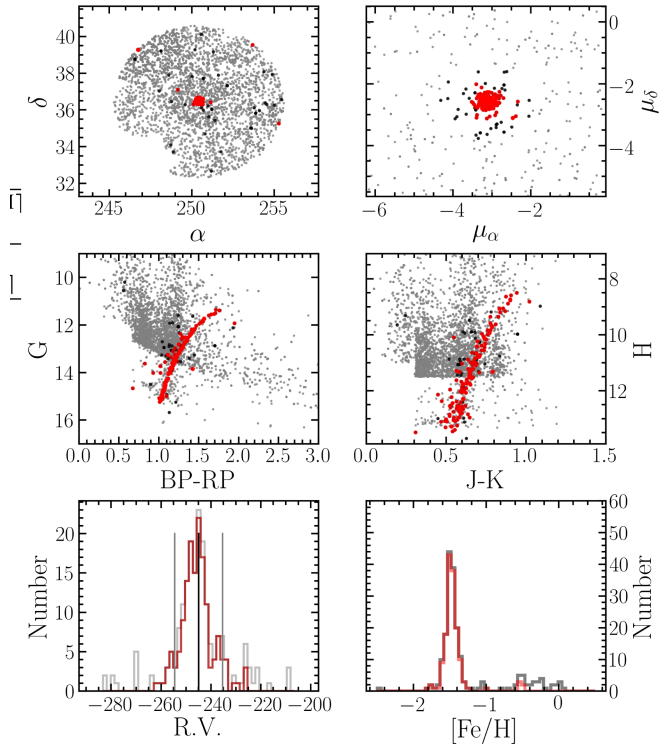
Figure 2. Selecting M13 members in the APOGEE catalogue. In all panels, grey dots represent catalogue stars within $4r_J$ of the GC centre. Black dots represent stars whose PMs differ from the mean value from the VB catalogue by no more than $4\sigma_{PV}$. Red dots represent a subsample of the former whose RVs differ from the GC mean by no more than $3\sigma_{RV}$.

structural parameters. The initial sample is obtained by extracting all sources with five- or six-parameter astrometric solutions from *Gaia* within a certain distance from the centre of each GC, which in the general case is taken to be a few times greater than the cluster half-light radius. A first run of mixture modelling in the 3D astrometric space is performed on a subset of the sources with the most reliable astrometry, where one of the Gaussian components represents the cluster and the remaining component(s) account for the field stars. A full mixture model is then run, where a Plummer model is adopted to match each GC's density profile, with the scale radius as a free parameter. The parameter space is explored with a Markov chain Monte Carlo (MCMC) code initialized with astrometric parameters determined by extreme deconvolution. Membership probabilities for each star are then determined following the convergence of the MCMC runs. Colour–magnitude diagrams of members thus obtained for each GC are inspected visually to verify the outcome of the mixture model, which did not utilize any of the photometric information. Finally, the mean parallax and PM of each cluster and their uncertainties are taken from the MCMC chain.

4.2 RV-based probabilities

Exceedingly accurate RVs are one of the main data products of the APOGEE survey. This can be verified through a quick comparison with the data from the latest *Gaia* release (Data Release 3 – DR3; Gaia Collaboration 2023). We cross-matched our sample for M13 with the *Gaia* DR3 catalogue, obtaining 108 matches. The mean heliocentric RV and rms scatter for each sample are in excellent agreement, with $\langle RV_{APO} \rangle = -246.30$ km s^{-1} and $\langle \sigma_{APO} \rangle = 5.27$ km s^{-1} for the APOGEE sample, and $\langle RV_{Gaia} \rangle =$

-246.33 km s^{-1} and $\langle \sigma_{Gaia} \rangle = 5.95$ km s^{-1}. It is noteworthy that the mean RVs agree to within 30 m s^{-1}, reflecting the great accuracy of the two data sets. In addition, the rms scatter, which results from the convolution between the cluster velocity dispersion and measurement error, is lower in the APOGEE sample by $\sim$12 per cent, reflecting APOGEE's superior RV precision.

We take advantage of this high-quality data set to complement the membership information available from the VB catalogue with RV-based membership probabilities. These probabilities were estimated as follows. We adopted a procedure similar to that of Gieseking (1985) whereby the RV distribution within the field of each GC was modelled as a combination of Gaussian functions plus a constant background. For any given star i, the RV-based membership probability is given by

$$p_i = \frac{G_{gc}(v_i)}{G_{gc}(v_i) + B(v_i)}, \tag{1}$$

where v_i is the radial velocity (RV) of the star, $G_{gc}(v)$ is the Gaussian function describing the RV distribution of the GC, and $B(v)$ is a function accounting for the RV distribution of the field background.

For well-sampled GCs, the functions $G_{gc}(v)$ and $B(v)$ were obtained from a fit to the RV distribution from the stars contained within the field of each GC. In cases where the GC is poorly sampled and/or the contrast with the background is poor, the $G_{gc}(v)$ function adopted was based on parameters (mean RV and velocity dispersion) gathered from the VB catalogue. The background function $B(v)$, in the general case, was a combination of Gaussians and a constant floor value. In no case were more than two Gaussians required to account for the background data. An example fit is shown in Fig. 5.

5 RESULTS AND SCIENCE HIGHLIGHTS

This VAC can be employed in a myriad of different science projects. We highlight a few aspects of the data base that illustrate its potential. In Fig. 6, selected elemental abundances sampling different nucleosynthetic pathways are displayed in various panels. Only abundances derived from spectra with S/N > 150 are shown. To distinguish stars associated with individual GCs, symbols are colour coded by heliocentric distance. The complexity of the GC member candidates distribution in chemical composition space is promptly evident from a first glance at these data.

In Fig. 7, the data for M5 (NGC 5904) are displayed on the [C/Fe] versus [N/Fe] plane, where symbols are colour coded by surface gravity (log g). Two sequences are clearly visible, where a gentle variation of N and C abundances can be seen to be correlated with log g. This variation is due to mixing along the giant branch, whereby more evolved stars (lower log g) display depleted C and enhanced N due to the progressive mixing of CNO-processed material during the evolution along the red giant branch. The more drastic variation associated with the MP phenomenon connects stars with the same log g between the two sequences (e.g. Phillips et al. 2022).

In Fig. 8, data for various GCs with [Fe/H] < -0.5 are displayed on the [Mg/Fe] versus [Al/Fe] plane. Symbols are colour coded by metallicity. Metal-poor GCs show a strong anticorrelation between these two elements. The various GC sequences are displaced relative to each other due to variations in the systems' natal chemical compositions, associated with their origin. The weakening of this anticorrelation with increasing metallicity (e.g. Nataf et al. 2019) manifests itself by the near absence of an anticorrelation in the most metal-rich GCs.
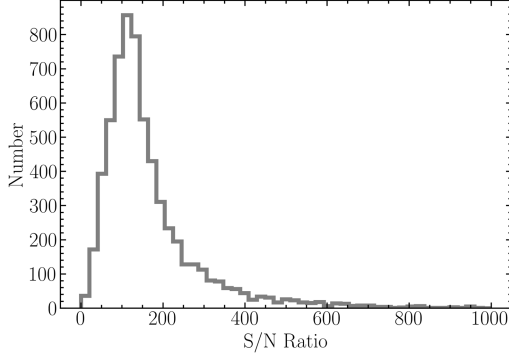
Figure 3. Distribution of the S/N pixel^{-1} of the resulting sample.

Finally, in Appendix A, we present a comparison of the APOGEE DR17 elemental abundances published in this VAC with data from various sources from the literature.

5.1 Extra-tidal candidates

GCs are slowly dissolving, shedding stars under the combined effect of evaporation and tidal stripping as they follow their orbits within the Milky Way dark matter halo. Evidence to this phenomenon has been documented as stars are detected beyond GC tidal radii, in the form of tidal streams (e.g. Odenkirchen et al. 2001; Belokurov et al. 2006; Grillmair & Johnson 2006; Bonaca & Hogg 2018; Malhan, Valluri & Freese 2021) and diffuse outer envelopes or less defined collections of
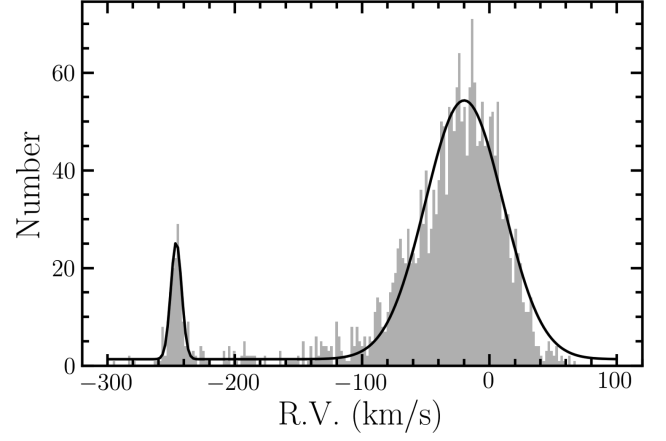
Figure 5. Fit of the RV distribution in the field of M13. The model fit is a double Gaussian with an additional constant background. The secondary peak corresponds to the RVs of the cluster.

extra-tidal stars (e.g. Kuzma et al. 2016; Kuzma, Da Costa & Mackey 2018; Chun, Lee & Lim 2020; Kundu et al. 2022; Piatti 2022).

Identifying extra-tidal stars is a difficult task requiring deep photometry over a wide field of view. More recently, data from the *Gaia* satellite have enabled the use of PMs for that purpose (e.g. Kundu, Minniti & Singh 2019). In the past decade, chemical tagging has been used to identify field stars with chemistry that is characteristic of GC populations (e.g. Martell & Grebel 2010; Lind
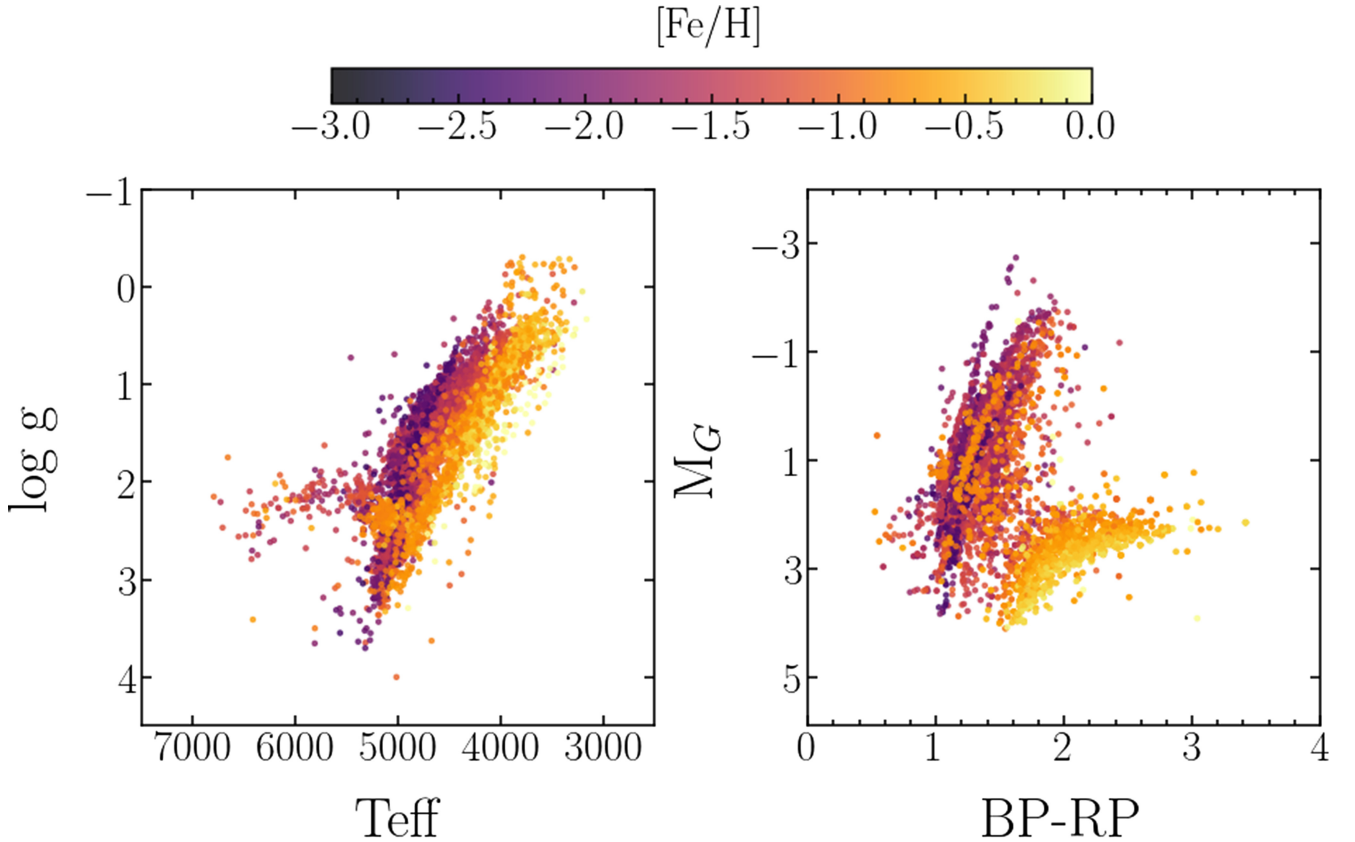
Figure 4. Right: Kiel diagram for the resulting sample. Note that this plot does not display all stars included in the catalogue, as ASPCAP failed to deliver stellar parameters for some stars. Left: *Gaia* EDR3 colour–magnitude diagram of the GC parent sample, including only stars with $A_K < 0.3$. In both panels, stars are colour coded by the APOGEE DR17 Fe abundances.
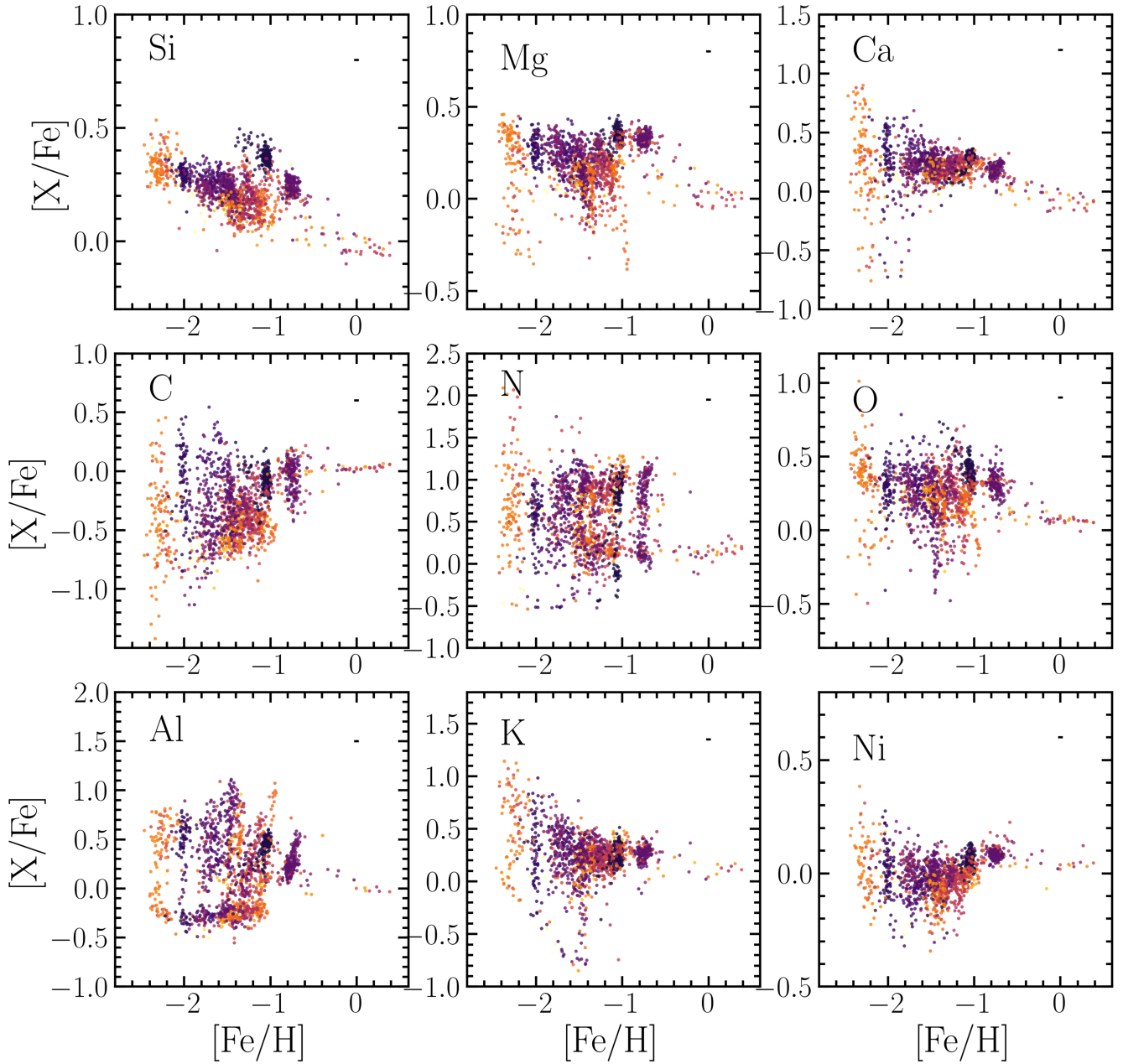
Figure 6. Sample elemental abundances for Galactic GCs included in the VAC. Only abundances derived from spectra with S/N > 150 are shown. To distinguish individual GCs, data are colour coded by the cluster heliocentric distance. GCs with large spreads in metallicity, namely ω Cen and M54, are excluded from this plot. Mean error bars are displayed on the top right of each panel.

et al. 2015; Martell et al. 2016; Fernández-Trincado et al. 2017; Schiavon et al. 2017a; Tang et al. 2019), leading up to moderately robust estimates of the contribution of dissolved GCs to the Milky Way stellar halo mass budget (e.g. Martell et al. 2011; Schiavon et al. 2017a; Koch, Grebel & Martell 2019; Horta et al. 2021).

Linking so-called 'N-rich' field stars with their parent GCs is quite important as a means to establish once and for all their GC origin (e.g. Kisku et al. 2021). However, such associations have proved difficult, resulting from likelihood estimates based on orbital parameters (e.g. Savino & Posti 2019).

Detailed chemistry and precision RVs for large samples combined with *Gaia*-quality astrometry and GC structural parameters can make an important contribution in this context. Large samples with pre-

cision chemistry enable unequivocal association of extra-tidal stars with their parent GCs. Indeed, recent work has provided evidence for the presence of N-rich stars beyond the Jacobi radius of M54 and Palomar 5 (Fernández-Trincado et al. 2021a; Phillips et al. 2022).

In Fig. 9, VAC data are displayed on various chemical planes. Data for the ω Cen and M54 are omitted from these plots. Grey dots show the whole sample, and black dots represent only stars located beyond the Jacobi radius of their parent GC. While most extra-tidal stars have normal chemistry, a few dozen N-rich stars can be identified in those planes, due to their enhanced abundances of N and Al, and depleted Mg and O. Extra-tidal stars can be easily identified in the VAC by the value of the parameter DPOS, which is equal to the angular distance to each GC centre, in units of r_J. Extra-tidal stars have DPOS > 1.
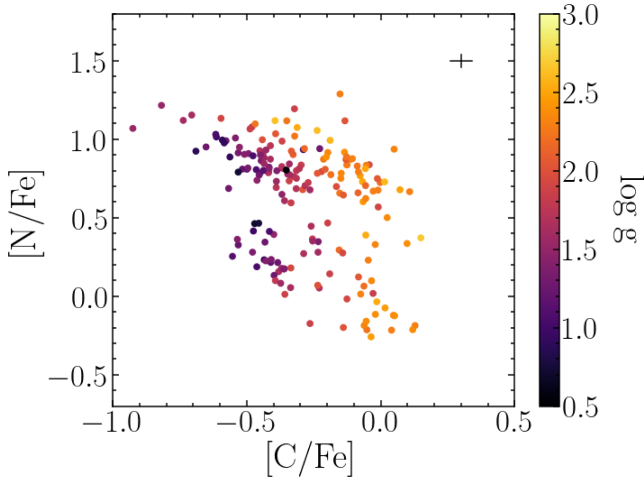
**Figure 7.** Carbon–nitrogen (C–N) anticorrelation in the GC M5 (NGC 5904). Symbols are colour coded by surface gravity (log g) to distinguish C–N abundance variations due to stellar evolution from those associated with the multiple populations' (MPs) phenomenon. Two diagonal sequences can be seen. Along each sequence, the variations of N and C abundances are correlated with log g, as deep mixing brings the by-products of the CNO cycle to the star's surface steadily changing its chemical composition during evolution along the giant branch. The more drastic anticorrelation due to the MP phenomenon connects stars with the same log g between the two sequences. Mean error bars are displayed on the top right.
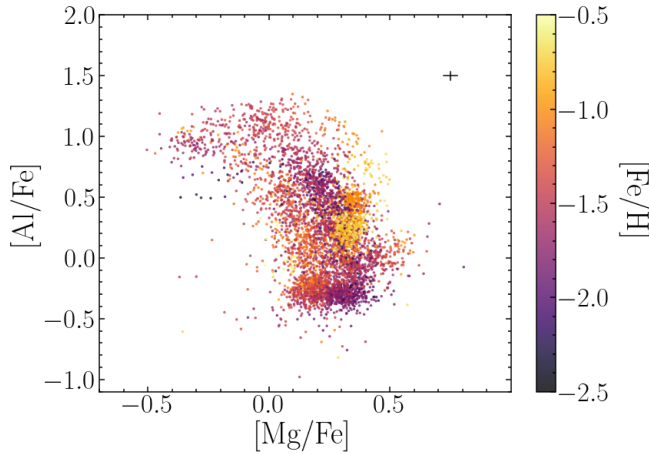

Figure 8. Magnesium–aluminium (Mg–Al) anticorrelation for a collection of GCs with [Fe/H] ≤ -0.5. Different sequences are displaced on this plane according to GC's natal chemical composition. The Mg–Al anticorrelation is weakened or even absent towards higher metallicity. Mean error bars are displayed on the top right.

5.1.1 The case of M54

M54 is the nuclear cluster of the Sagittarius dwarf Spheroidal (Sgr dSph). Its chemodynamical properties have been studied extensively (e.g. Law & Majewski 2010; Mucciarelli et al. 2017) and merit some attention. In Fig. 10, we show the data for M54 members on the same chemical planes as Fig. 9. Top/bottom panels show intra-/extra-tidal stars. It is noteworthy that this cluster is characterized by a very large population of extra-tidal stars, some of which have N-rich abundance patterns (see e.g. Fernández-Trincado et al. 2021a). Indeed, a large fraction of the entire population of extra-tidal stars identified in this work are associated with M54. That could be a result of the cluster's undergoing severe tidal disruption under
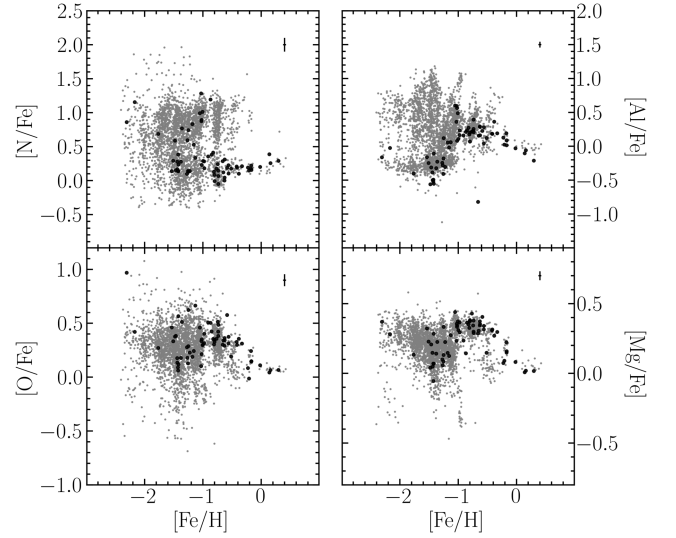

Figure 9. Candidate GC members in various chemical planes. Stars within their parent GC Jacobi radii are shown as grey symbols, whereas extra-tidal stars are displayed as black dots. A substantial fraction of the extra-tidal stars have N-rich abundance patterns, confirming the GC origin of N-rich stars identified in previous studies. For previous identifications of extra-tidal N-rich stars see discussion in text. Mean error bars are displayed on the top right of each panel.
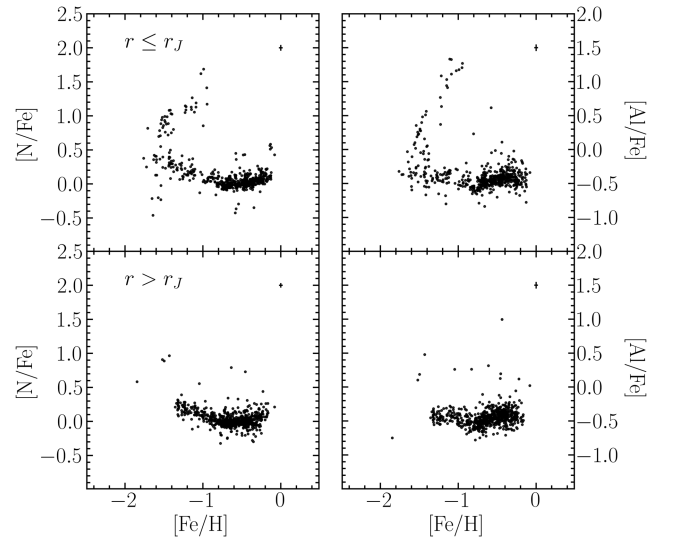
Figure 10. Candidate members of M54 (NGC 6715), the nuclear cluster of the Sagittarius dwarf Spheroidal (Sgr dSph), on the N–Fe and Al–Fe chemical planes. Stars located within (top panel) or beyond (bottom) the cluster's Jacoby radius are displayed. Note the large number of extra-tidal N-rich and/or Al-rich stars (bottom panel). It is not clear whether this effect is real or due to an underestimate of M54's Jacobi radius. Mean error bars are displayed on the top right of each panel.

the MW potential, or rather reflect a possible underestimate of the M54's Jacobi radius. Such estimates are plagued by considerable uncertainties. In the case of M54, the situation is made worse by the fact that it is not known whether the cluster is positioned at the centre of its host galaxy's potential well, and whether it possesses its own dark matter halo (e.g. Carlberg & Grillmair 2022). In view of these uncertainties, we decided to retain a large number of M54 candidate members, while acknowledging the reality that this sample
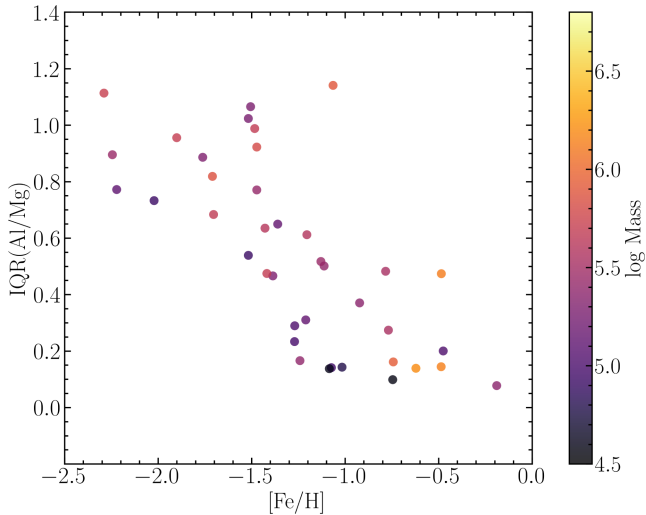
Figure 11. Interquartile range (IQR) of the [Al/Mg] ratio plotted against GC metallicity. A remarkable anticorrelation between the two quantities is apparent, with high significance ($\rho_x = -0.76$). Symbols are colour coded by log GC mass, but no correlation is apparent.

is considerably contaminated by Sgr dSph field stars. The catalogue users are again provided with data they can use to select subsamples according to their science goals.

### 5.2 Abundance spreads and global parameters

As discussed in the Introduction, perhaps the most puzzling observational feature of GCs is the presence of large anticorrelated spreads of the abundances of light elements. Despite many efforts from various groups, no particular scenario has been able to account for this phenomenon in a quantitative fashion (see review by Bastian & Lardo 2018). Naturally, correlations between chemical composition spreads and GC global parameters can provide valuable constraints on formation models. In this section, we provide a brief foray into the topic, exploring how this new catalogue can potentially contribute to this discussion. We focus on Al spreads. Aluminium abundances are exceptionally well measured in APOGEE spectra, over a wide range of metallicities. Moreover, unlike nitrogen, aluminium spreads can be assessed in a fairly unambiguous way, since the abundance of this element is not affected by stellar evolution effects.

Following Carretta et al. (2010), who adopted the [O/Na] interquartile range (IQR) as a measure of abundance spreads, we measure the IQR of the [Al/Mg] ratio. We first examine the well-known anticorrelation of aluminium spreads with GC metallicity (see also Nataf et al. 2019; Mészáros et al. 2020). The data are displayed in Fig. 11, where a very clear anticorrelation between IQR(Al/Mg) and [Fe/H] is present, with a Spearman's rank correlation coefficient $\rho_x = -0.76$. This result confirms previous studies reporting a substantial decrease of Al spreads in high-metallicity GCs. Symbols are colour coded by GC mass, but no clear correlation with that parameter can be seen.

Next, we examine the presence of a correlation between abundance spreads and a quantity related to a GC's gravitational potential. Such a correlation is interesting, as it may be an indication of the presence of chemical enrichment brought about by a history of feedback-regulated star formation (see also Carretta et al. 2010; Schiavon et al. 2013; Sakari et al. 2016). In Fig. 12, we plot IQR(Al/Mg) against central escape velocity, from the VB catalogue. Because the
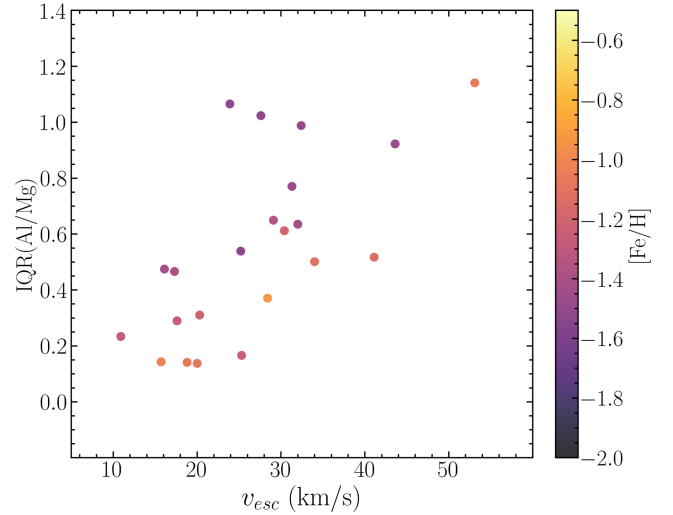
Figure 12. IQR of the [Al/Mg] ratio plotted against central escape velocity. A strong correlation is present ($\rho_x = 0.68$), but only after controlling for the effect of metallicity. Only GCs with $-1.7 <$ [Fe/H] < -0.8 are considered. Symbols are colour coded by [Fe/H]. This might be an indicator of chemical enrichment due to a history of feedback-regulated star formation.
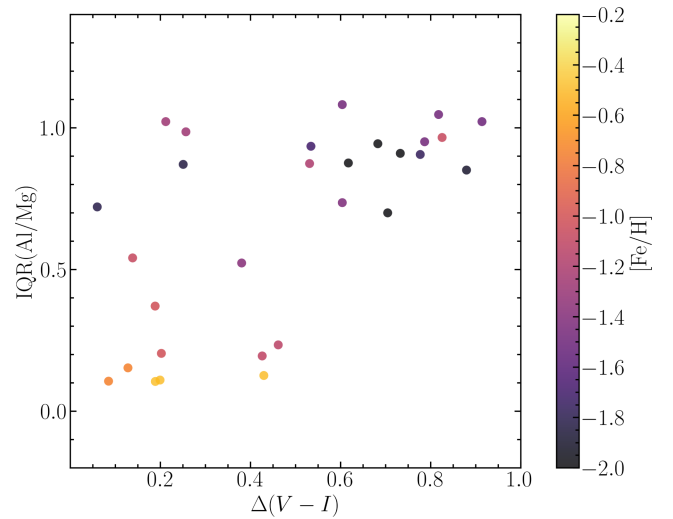
Figure 13. IQR of the [Al/Mg] ratio plotted against a horizontal branch (HB) morphology parameter, $\Delta(V - I)$, which is higher for bluer HB morphologies. A fairly strong correlation is present ($\rho_x = 0.63$), in the sense that only GCs with high IQR(Al/Mg) present a blue HB. Although GCs with red HBs can also have high IQR(Al/Mg), all GCs with low IQR(Al/Mg) have red HBs.

correlation between IQR(Al/Mg) and metallicity is so strong, we must control for this parameter, so only GCs with $-1.7 <$ [Fe/H] < -0.8 are shown. A strong correlation is seen ($\rho_x = 0.68$). We also find a strong correlation with central velocity dispersion ($\rho_x = 0.69$) and GC mass ($\rho_x = 0.62$).

We conclude by inspecting the relation between abundance spread and horizontal branch (HB) morphology. A correlation between these observables is expected because the morphology of the HB is in part dictated by the abundance of helium, an element for which there is strong evidence for abundance spreads (e.g. Renzini 2008). In the following, we adopt IQR(Al/Mg) as a surrogate for a spread in the abundance of helium. The data are displayed in Fig. 13, where IQR(Al/Mg) is plotted against the $\Delta(V - I)$ parameter from

Dotter et al. (2010). High values of $\Delta(V-I)$ correspond to blue HB morphology. Although we find a relatively high Spearman's rank correlation coefficient ($\rho_x = 0.63$), the data behave in a subtle way. There is a zone of avoidance at low IQR(Al/Fe) and blue HB morphology. GCs with large abundance spreads can have either a red or a blue HB, but those with low spreads are all characterized by a red HB. This may be related to the fact that the morphology of the HB is affected by a number of parameters besides He abundance, including age, binarity, and mass loss during the first-ascent red giant branch phase.

6 THE CATALOGUE

The VAC presented in this paper consists of two files in FITS format. The catalogue itself is contained in file VAC_GC_DR17_synspec_rev1.fits, which includes all the data from the APOGEE DR17 allStar-dr17-synspec_rev1.fits for each of the 7737 entries associated with GC candidate members. This file also incorporates distances from GC centres (in units of r_J), residual PMs, RVs, and [Fe/H], in units of the rms dispersions of those values. Two sets of membership probabilities are also provided, those based on the RV analysis in Section 4.2 and those from the VB catalogue, when available. Another file named GC_parameters_VAC.fits contains, for each GC, the mean and rms values for RVs, PMs, and metallicities, as well as a number of global parameters from the literature. Both files are available for download from the SDSS DR17 VAC webpage (https://www.sdss4.org/dr17/data_access/value-addedcatalogs/).

ACKNOWLEDGEMENTS

RPS dedicates this paper to the memory of Professor José Augusto Buarque de Nazareth. The authors wish to thank workers in the health and services industry who made it possible for this work to be conducted from home during challenging pandemic years. DM is supported by ANID BASAL projects ACE210002 and FB210003, and by FONDECYT Project No. 1220724. JGF-T gratefully acknowledges the grant support provided by Proyecto FONDECYT Iniciación No. 11220340, from ANID Concurso de Fomento a la Vinculación Internacional para Instituciones de Investigación Regionales (Modalidad corta duración) Proyecto No. FOVI210020, from the ESO – Government of Chile Joint Committee 2021 (ORP 023/2021), and from Becas Santander Movilidad Internacional Profesores 2022, Banco Santander Chile. TCB acknowledges partial support from grant PHY 14–30152, Physics Frontier Center/JINA Center for the Evolution of the Elements (JINA-CEE), and from OISE-1927130: The International Research Network for Nuclear Astrophysics (IReNA), awarded by the U.S. National Science Foundation. Funding for the Sloan Digital Sky Survey IV has been provided by the Alfred P. Sloan Foundation, the U.S. Department of Energy Office of Science, and the Participating Institutions. SDSS acknowledges support and resources from the Center for High-Performance Computing at the University of Utah. The SDSS website is www.sdss.org. SDSS is managed by the Astrophysical Research Consortium for the Participating Institutions of the SDSS Collaboration including the Brazilian Participation Group, the Carnegie Institution for Science, Carnegie Mellon University, the Chilean Participation Group, the French Participation Group, Harvard-Smithsonian Center for Astrophysics, Instituto de Astrofísica de Canarias, The Johns Hopkins University, Kavli Institute for the Physics and Mathematics of the Universe (IPMU)/University of Tokyo, the Korean Participation Group, Lawrence Berkeley National Laboratory, Leibniz Institut für Astrophysik Potsdam (AIP), Max-Planck-Institut für Astronomie (MPIA Heidelberg), Max-Planck-Institut für Astrophysik (MPA Garching), Max-Planck-Institut für Extraterrestrische Physik (MPE), National Astronomical Observatories of China, New Mexico State University, New York University, University of Notre Dame, Observatório Nacional/MCTI, The Ohio State University, Pennsylvania State University, Shanghai Astronomical Observatory, United Kingdom Participation Group, Universidad Nacional Autónoma de México, University of Arizona, University of Colorado Boulder, University of Oxford, University of Portsmouth, University of Utah, University of Virginia, University of Washington, University of Wisconsin, Vanderbilt University, and Yale University.

This work presents results from the European Space Agency (ESA) space mission *Gaia*. *Gaia* data are being processed by the *Gaia* Data Processing and Analysis Consortium (DPAC). Funding for the DPAC is provided by national institutions, in particular the institutions participating in the *Gaia* MultiLateral Agreement (MLA). The *Gaia* mission website is https://www.cosmos.esa.int/gaia. The *Gaia* archive website is https://archives.esac.esa.int/gaia.

Software used: ASTROPY (Astropy Collaboration 2013; Price-Whelan et al. 2018), SCIPY (Virtanen et al. 2020), NUMPY (Oliphant 2006), MATPLOTLIB (Hunter 2007), GALPY (Bovy 2015; Mackereth & Bovy 2018), and TOPCAT (Taylor 2005).

Facilities: Sloan Foundation 2.5-m Telescope of Apache Point Observatory (APOGEE-North), Irénée du Pont 2.5-m Telescope of Las Campanas Observatory (APOGEE-South), *Gaia* satellite/European Space Agency (*Gaia*).

DATA AVAILABILITY

All data used in this paper are publicly available at the SDSS-IV DR17 website: http://www.sdss.org/dr17/.

REFERENCES

Abdurro'uf et al., 2022, ApJS, 259, 35
Allende Prieto C., Beers T. C., Wilhelm R., Newberg H. J., Rockosi C. M., Yanny B., Lee Y. S., 2006, ApJ, 636, 804
Armandroff T. E., Zinn R., 1988, AJ, 96, 92
Ashman K. M., Zepf S. E., 1992, ApJ, 384, 50
Astropy Collaboration, 2013, A&A, 558, A33
Barbuy B., Bica E., Ortolani S., 1998, A&A, 333, 117
Bastian N., Lardo C., 2018, ARA&A, 56, 83
Baumgardt H., Vasiliev E., 2021, MNRAS, 505, 5957
Beaton R. L. et al., 2021, AJ, 162, 302
Bekki K., Freeman K. C., 2003, MNRAS, 346, L11
Belokurov V., Evans N. W., Irwin M. J., Hewett P. C., Wilkinson M. I., 2006, ApJ, 637, L29
Belokurov V., Erkal D., Evans N. W., Koposov S. E., Deason A. J., 2018, MNRAS, 478, 611
Bica E., Alloin D., 1986, A&A, 162, 21
Blanton M. R. et al., 2017, AJ, 154, 28
Bolte M., Hogan C. J., 1995, Nature, 376, 399
Bonaca A., Hogg D. W., 2018, ApJ, 867, 101
Bovy J., 2015, ApJS, 216, 29
Bowen I. S., Vaughan A. H. J., 1973, Appl. Opt., 12, 1430
Briley M. M., Smith V. V., King J., Lambert D. L., 1997, AJ, 113, 306
Brodie J. P., Strader J., 2006, ARA&A, 44, 193
Buder S. et al., 2022, MNRAS, 510, 2407
Caldwell N., Harding P., Morrison H., Rose J. A., Schiavon R., Kriessler J., 2009, AJ, 137, 94
Callingham T. M., Cautun M., Deason A. J., Frenk C. S., Grand R. J. J., Marinacci F., 2022, MNRAS, 513, 4107
Cannon R. D., Croke B. F. W., Bell R. A., Hesser J. E., Stathakis R. A., 1998, MNRAS, 298, 601
Carlberg R. G., Grillmair C. J., 2022, ApJ, 935, 14
Carretta E., Gratton R. G., 1997, A&AS, 121, 95
Carretta E., Bragaglia A., Gratton R., Lucatello S., 2009, A&A, 505, 139

Carretta E., Bragaglia A., Gratton R. G., Recio-Blanco A., Lucatello S., D'Orazi V., Cassisi S., 2010, A&A, 516, A55

Castellani V., degl'Innocenti S., 1999, A&A, 344, 97

Cavallo R. M., Nagar N. M., 2000, AJ, 120, 1364

Chiosi C., Bertelli G., Bressan A., 1992, ARA&A, 30, 235

Choksi N., Gnedin O. Y., Li H., 2018, MNRAS, 480, 2343

Chun S.-H., Lee J.-J., Lim D., 2020, ApJ, 900, 146

Cohen J. G., Meléndez J., 2005, AJ, 129, 303

Cohen R. E., Moni Bidin C., Mauro F., Bonatto C., Geisler D., 2017, MNRAS, 464, 1874

Cunha K. et al., 2017, ApJ, 844, 145

Denissenkov P. A., Weiss A., 1996, A&A, 308, 773

De Silva G. M. et al., 2015, MNRAS, 449, 2604

Dotter A. et al., 2010, ApJ, 708, 698

Fall S. M., Rees M. J., 1985, ApJ, 298, 18

Fernández-Trincado J. G. et al., 2017, ApJ, 846, L2

Fernández-Trincado J. G. et al., 2021a, A&A, 648, A70

Fernández-Trincado J. G. et al., 2021b, ApJ, 908, L42

Fernández-Trincado J. G., Minniti D., Garro E. R., Villanova S., 2022, A&A, 657, A84

Forbes D. A., 2020, MNRAS, 493, 847

Gaia Collaboration, 2021, A&A, 649, A1

Gaia Collaboration, 2023, A&A, 674, A1

Galleti S., Bellazzini M., Federici L., Buzzoni A., Fusi Pecci F., 2007, A&A, 471, 127

García Pérez A. E. et al., 2016, AJ, 151, 144

Geisler D. et al., 2021, A&A, 652, A157

Gieseking F., 1985, A&AS, 61, 75

Gratton R. G., Carretta E., Bragaglia A., 2012, A&AR, 20, 50

Grillmair C. J., Johnson R., 2006, ApJ, 639, L17

Gunn J. E. et al., 2006, AJ, 131, 2332

Gustafsson B., Edvardsson B., Eriksson K., Jørgensen U. G., Nordlund Å., Plez B., 2008, A&A, 486, 951

Hasselquist S. et al., 2016, ApJ, 833, 81

Helmi A., Babusiaux C., Koppelman H. H., Massari D., Veljanoski J., Brown A. G. A., 2018, Nature, 563, 85

Holtzman J. A. et al., 2015, AJ, 150, 148

Holtzman J. A. et al., 2018, AJ, 156, 125

Horta D. et al., 2020, MNRAS, 493, 3363

Horta D. et al., 2021, MNRAS, 500, 5462

Hubeny I., Lanz T., 2017, preprint (arXiv:1706.01859)

Hunter J. D., 2007, Comput. Sci. Eng., 9, 90

Ivans I. I., Kraft R. P., Sneden C., Smith G. H., Rich R. M., Shetrone M., 2001, AJ, 122, 1438

Johnson C. I., Pilachowski C. A., 2010, ApJ, 722, 1373

Johnson C. I., Pilachowski C. A., 2012, ApJ, 754, L38

Johnson C. I., Kraft R. P., Pilachowski C. A., Sneden C., Ivans I. I., Benman G., 2005, PASP, 117, 1308

Jönsson H. et al., 2018, AJ, 156, 126

Jönsson H. et al., 2020, AJ, 160, 120

Kamann S. et al., 2018, MNRAS, 473, 5591

Kisku S. et al., 2021, MNRAS, 504, 1657

Koch A., McWilliam A., 2010, AJ, 139, 2289

Koch A., Grebel E. K., Martell S. L., 2019, A&A, 625, A75

Kraft R. P., 1979, ARA&A, 17, 309

Kraft R. P., 1994, PASP, 106, 553

Kraft R. P., Ivans I. I., 2003, PASP, 115, 143

Kraft R. P., Sneden C., Langer G. E., Prosser C. F., 1992, AJ, 104, 645

Kruijssen J. M. D., 2015, MNRAS, 454, 1658

Kruijssen J. M. D., Pfeffer J. L., Reina-Campos M., Crain R. A., Bastian N., 2019, MNRAS, 486, 3180

Kundu R., Minniti D., Singh H. P., 2019, MNRAS, 483, 1737

Kundu R., Navarrete C., Sbordone L., Carballo-Bello J. A., Fernández-Trincado J. G., Minniti D., Singh H. P., 2022, A&A, 665, A8

Kuzma P. B., Da Costa G. S., Mackey A. D., Roderick T. A., 2016, MNRAS, 461, 3639

Kuzma P. B., Da Costa G. S., Mackey A. D., 2018, MNRAS, 473, 2881

Lai D. K., Smith G. H., Bolte M., Johnson J. A., Lucatello S., Kraft R. P., Sneden C., 2011, AJ, 141, 62

Law D. R., Majewski S. R., 2010, ApJ, 718, 1128

Lee J.-W., Carney B. W., Balachandran S. C., 2004, AJ, 128, 2388

Lind K., Korn A. J., Barklem P. S., Grundahl F., 2008, A&A, 490, 777

Lind K. et al., 2015, A&A, 575, L12

Mackereth J. T., Bovy J., 2018, PASP, 130, 114501

Majewski S. R., Nidever D. L., Smith V. V., Damke G. J., Kunkel W. E., Patterson R. J., Bizyaev D., García Pérez A. E., 2012, ApJ, 747, L37

Majewski S. R. et al., 2017, AJ, 154, 94

Malhan K., Valluri M., Freese K., 2021, MNRAS, 501, 179

Martell S. L., Grebel E. K., 2010, A&A, 519, A14

Martell S. L., Smolinski J. P., Beers T. C., Grebel E. K., 2011, A&A, 534, A136

Martell S. L. et al., 2016, ApJ, 825, 146

Martell S. L. et al., 2017, MNRAS, 465, 3203

Massari D., Koppelman H. H., Helmi A., 2019, A&A, 630, L4

Masseron T. et al., 2019, A&A, 622, A191

Meléndez J., Cohen J. G., 2009, ApJ, 699, 2017

Mészáros S. et al., 2012, AJ, 144, 120

Mészáros S. et al., 2015, AJ, 149, 153

Mészáros S. et al., 2020, MNRAS, 492, 1641

Mészáros S. et al., 2021, MNRAS, 505, 1645

Milone A. P., Marino A. F., 2022, Universe, 8, 359

Minniti D., Peterson R. C., Geisler D., Claria J. J., 1996, ApJ, 470, 953

Minniti D. et al., 2017, ApJ, 849, L24

Mucciarelli A., Bellazzini M., Ibata R., Romano D., Chapman S. C., Monaco L., 2017, A&A, 605, A46

Myeong G. C., Vasiliev E., Iorio G., Evans N. W., Belokurov V., 2019, MNRAS, 488, 1235

Nataf D. M. et al., 2019, AJ, 158, 14

Nidever D. L. et al., 2015, AJ, 150, 173

O'Connell J. E., Johnson C. I., Pilachowski C. A., Burks G., 2011, PASP, 123, 1139

Odenkirchen M. et al., 2001, ApJ, 548, L165

Oliphant T., 2006, A Guide to NumPy. Trelgol Publishing, Provo, UT

Osorio Y., Allende Prieto C., Hubeny I., Mészáros S., Shetrone M., 2020, A&A, 637, A80

Otsuki K., Honda S., Aoki W., Kajino T., Mathews G. J., 2006, ApJ, 641, L117

Pancino E., Pasquini L., Hill V., Ferraro F. R., Bellazzini M., 2002, ApJ, 568, L101

Pfeffer J., Kruijssen J. M. D., Crain R. A., Bastian N., 2018, MNRAS, 475, 4309

Pfeffer J., Lardo C., Bastian N., Saracino S., Kamann S., 2021, MNRAS, 500, 2514

Phillips S. G. et al., 2022, MNRAS, 510, 3727

Piatti A. E., 2022, MNRAS, 514, 4982

Piotto G. et al., 2002, A&A, 391, 945

Price-Whelan A. M. et al., 2018, AJ, 156, 123

Puzia T. H., Saglia R. P., Kissler-Patig M., Maraston C., Greggio L., Renzini A., Ortolani S., 2002, A&A, 395, 45

Ramírez S. V., Cohen J. G., 2002, AJ, 123, 3277

Ramírez S. V., Cohen J. G., 2003, AJ, 125, 224

Renzini A., 2008, MNRAS, 391, 354

Renzini A., Fusi Pecci F., 1988, ARA&A, 26, 199

Renzini A. et al., 2015, MNRAS, 454, 4197

Roederer I. U., Sneden C., 2011, AJ, 142, 22

Rosenberg A., Piotto G., Saviane I., Aparicio A., 2000, A&AS, 144, 5

Sahu S. et al., 2022, MNRAS, 514, 1122

Sakari C. M. et al., 2016, ApJ, 829, 116

Salaris M., Weiss A., 2002, A&A, 388, 492

Salaris M., Cassisi S., Weiss A., 2002, PASP, 114, 375

Sandage A., 1970, ApJ, 162, 841

Santana F. A. et al., 2021, AJ, 162, 303

Sarajedini A. et al., 2007, AJ, 133, 1658

Savino A., Posti L., 2019, A&A, 624, L9

Schiavon R. P., Rose J. A., Courteau S., MacArthur L. A., 2005, ApJS, 160, 163

Schiavon R. P. et al., 2012, AJ, 143, 121

Schiavon R. P., Caldwell N., Conroy C., Graves G. J., Strader J., MacArthur L. A., Courteau S., Harding P., 2013, ApJ, 776, L7

Schiavon R. P. et al., 2017a, MNRAS, 465, 501

Schiavon R. P. et al., 2017b, MNRAS, 466, 1010

Schwarzschild M., 1970, QJRAS, 11, 12

Schweizer F., 1987, in Faber S. M., ed., Nearly Normal Galaxies: From the Planck Time to the Present. Springer-Verlag, New York, p. 18

Searle L., Zinn R., 1978, ApJ, 225, 357

Shapley H., 1918, ApJ, 48, 154

Shetrone M. D., 1996, AJ, 112, 1517

Shetrone M. et al., 2015, ApJS, 221, 24

Smith G. H., Shetrone M. D., Strader J., 2007, PASP, 119, 722

Smith V. V. et al., 2021, AJ, 161, 254

Sneden C., Kraft R. P., Prosser C. F., Langer G. E., 1991, AJ, 102, 2001

Sneden C., Kraft R. P., Prosser C. F., Langer G. E., 1992, AJ, 104, 2121

Sneden C., Kraft R. P., Shetrone M. D., Smith G. H., Langer G. E., Prosser C. F., 1997, AJ, 114, 1964

Sneden C., Pilachowski C. A., Kraft R. P., 2000, AJ, 120, 1351

Sneden C., Kraft R. P., Guhathakurta P., Peterson R. C., Fulbright J. P., 2004, AJ, 127, 2162

Sobeck J. S. et al., 2011, AJ, 141, 175

Stetson P. B., Pancino E., Zocchi A., Sanna N., Monelli M., 2019, MNRAS, 485, 3042

Tang B., Liu C., Fernández-Trincado J. G., Geisler D., Shi J., Zamora O., Worthey G., Moreno E., 2019, ApJ, 871, 58

Taylor M. B., 2005, in Shopbell P., Britton M., Ebert R., eds, ASP Conf. Ser. Vol. 347, Astronomical Data Analysis Software and Systems XIV. Astron. Soc. Pac., San Francisco, p. 29

Usher C. et al., 2017, MNRAS, 468, 3828

Vasiliev E., Baumgardt H., 2021, MNRAS, 505, 5978

Virtanen P. et al., 2020, Nat. Methods, 17, 261

Wilson J. C. et al., 2019, PASP, 131, 055001

Yong D., Aoki W., Lambert D. L., 2006a, ApJ, 638, 1018

Yong D., Aoki W., Lambert D. L., Paulson D. B., 2006b, ApJ, 639, 918

Yong D., Karakas A. I., Lambert D. L., Chieffi A., Limongi M., 2008, ApJ, 689, 1031

Zamora O. et al., 2015, AJ, 149, 181

Zasowski G. et al., 2013, AJ, 146, 81

Zasowski G. et al., 2017, AJ, 154, 198

Zinn R., West M. J., 1984, ApJS, 55, 45

APPENDIX A: COMPARISON WITH DATA FROM THE LITERATURE

Elemental abundance analysis is a tricky procedure with outputs that depend strongly on a number of factors. On the empirical side, the results are sensitive to the choice of spectral region and the overall quality of the observational data, usually quantified in terms of S/N, resolution, and sampling. In addition, the adequacy of data reduction methods is critical, with details such as sky subtraction and telluric absorption elimination being particularly relevant in the NIR. The outcome is also strongly influenced by the arsenal employed in the analysis, including model atmospheres, line opacities (wavelengths, molecular and atomic excitation/ionization potentials, log gfs, damping constants), spectrum synthesis code, microturbulent velocities, and assumptions such as spherical symmetry versus plane-parallel atmospheres, and consideration or not of LTE. In modern times, the advent of massive surveys brought to the fore the automation of the core of the spectral analysis, introducing additional uncertainties. It is thus parred for the course that the fidelity of any new data set is scrutinized via comparison with numbers generated independently.
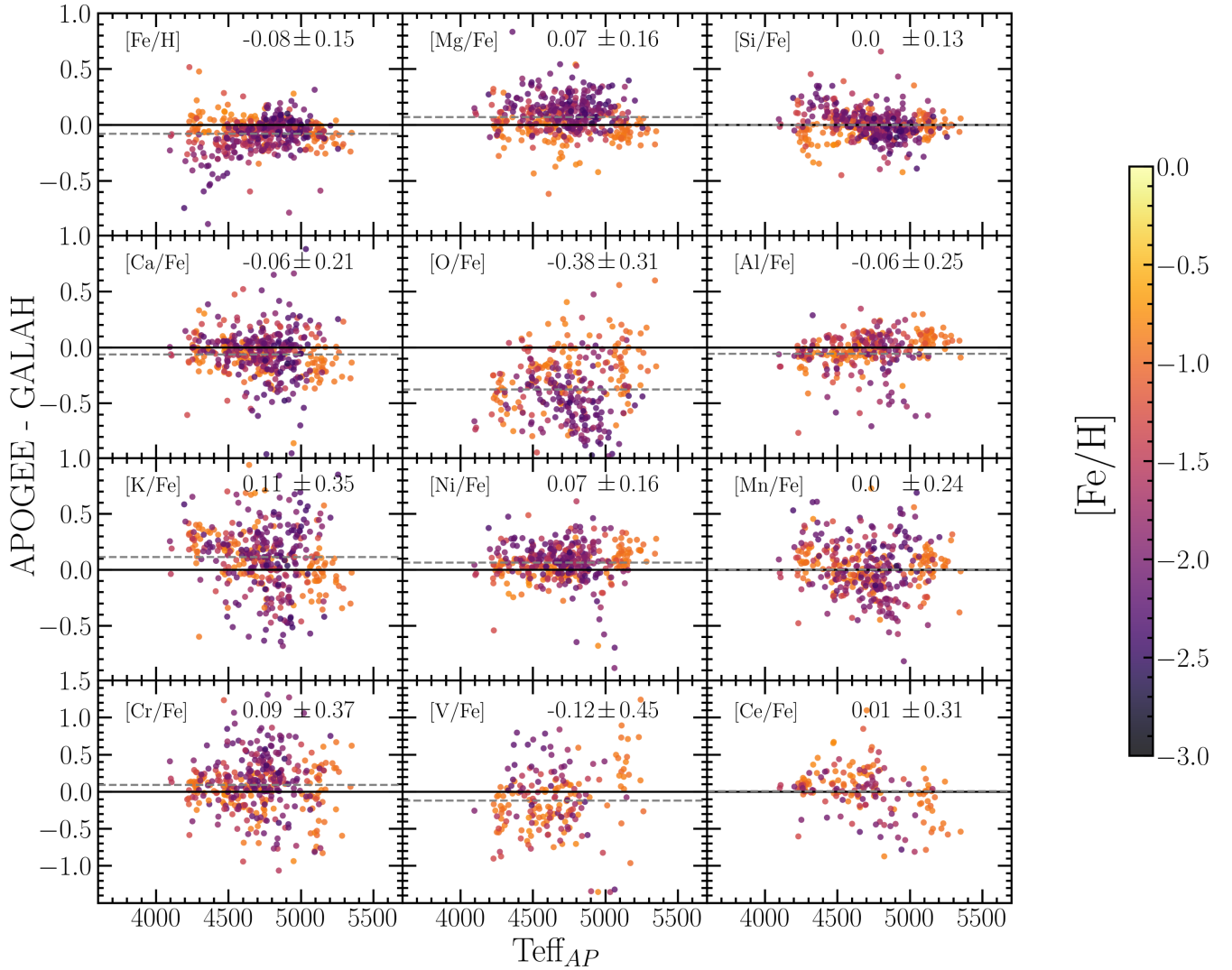
Table A1. Comparison of abundances from APOGEE and GALAH. Column information: (1) iron abundance or abundance ratio; (2) mean residual and rms dispersion around the mean; (3) intrinsic rms of APOGEE data; (4) intrinsic rms of GALAH data; and (5) number of stars in common.

Abundance (1)	Residual (2)	$\sigma_{\rm APO}$ (3)	$\sigma_{\rm GAL}$ (4)	$n_\star$ (5)
⌈Fe/H⌉	-0.08 ± 0.15	0.44	0.44	447
⌈Mg/Fe⌉	0.07 ± 0.16	0.14	0.21	423
⌈Si/Fe⌉	0.00 ± 0.13	0.07	0.13	441
⌈Ca/Fe⌉	-0.06 ± 0.21	0.16	0.17	417
⌈O/Fe⌉	-0.38 ± 0.31	0.15	0.33	317
⌈Al/Fe⌉	-0.06 ± 0.25	0.33	0.33	294
⌈K/Fe⌉	0.11 ± 0.35	0.25	0.25	395
⌈Ni/Fe⌉	0.07 ± 0.16	0.09	0.15	398
⌈Mn/Fe⌉	0.00 ± 0.24	0.20	0.18	365
⌈Cr/Fe⌉	0.09 ± 0.37	0.33	0.19	380
⌈V/Fe⌉	-0.12 ± 0.45	0.27	0.35	188
⌈Ce/Fe⌉	0.00 ± 0.24	0.40	0.33	165

APOGEE data have been regularly contrasted with literature values. The survey was indeed designed so as to afford such detailed comparisons, which were performed for each successive data release, and published in a number of papers (e.g. Holtzman et al. 2015, 2018; Mészáros et al. 2015, 2020, 2021; Jönsson et al. 2018, 2020; Nataf et al. 2019). To our knowledge, however, such a detailed examination of DR17 data has not yet been published, particularly within the regime of GCs, whose stars inhabit unique loci of chemical composition space. We briefly examine in this appendix a few comparisons with data from a large survey and those from other smaller independent studies.

We start by comparing our numbers with those generated by the GALactic Archaeology with HERMES (GALAH) survey (De Silva et al. 2015; Martell et al. 2017). For that purpose, we matched our sample stars with the GALAH DR3 catalogue (Buder et al. 2022), retaining only the elemental abundances with quality flag = 0, which yielded several hundred stars in common for all abundances of interest. The comparisons are displayed in Fig. A1, and the relevant statistics are listed in Table A1. Perfect agreement is indicated by the solid black line, whereas the mean difference is marked by the grey dashed line. Mean residuals and rms dispersion are indicated on the top right of each panel. Data points are colour coded by [Fe/H]. For all abundances, the mean residuals are well within the rms, except for the case of oxygen, for which the mean residuals are just above 1σ off. It is also noteworthy that for some elements, such as O, K, Cr, V, and Ce, the dispersion of the abundance ratio residuals is particularly large.

By looking at the intrinsic dispersion of the abundance ratios in the two data sets, we can pinpoint which of them contributes more importantly to the scatter in the data. Columns (3) and (4) of Table A1 display the numbers, obtained by simply calculating the rms of the abundances from APOGEE and GALAH, using only the stars in common for a fair assessment. For Mg, Si, O, and Ni the intrinsic scatter in the GALAH data is up to twice larger than APOGEE. The opposite is the case for Cr and, to some extent, Ce. For all the other elements, including those for which a large intrinsic scatter renders the comparison somewhat difficult to interpret (Fe and Al), the two sets have comparable dispersion. We conclude that for most elements involved in this comparison, the precision of the APOGEE data is superior to that of GALAH, within this restricted data set. By the same token, for all elements except oxygen, the zero-points of the two abundance systems are indistinguishable from each other.

Figure A1. Comparison between elemental abundances for stars in common between APOGEE and GALAH surveys, colour coded by [Fe/H]. The solid horizontal lines indicate identical abundances, whereas the dashed grey lines mark the position of the mean residuals. For all elements, except for oxygen, the mean residuals are much smaller than the rms of the distribution.

To address the matter of data accuracy, we need to resort to comparisons with other literature values based on classical abundance analysis of high-resolution (predominantly optical) spectra. The best place to start is the extensive data set painstakingly amassed over the years by E. Carretta and collaborators. The compilation presented by Carretta et al. (2010) focuses on Fe, O, and Na, but we limit our discussion to the former two elements. APOGEE abundances for Na are known to suffer from important shortcomings in the metallicity regime of interest, as they are based on only two lines that are weak in the spectra of metal-poor giants. Moreover, they are affected by important contamination by airglow emission (Jönsson et al. 2020).

Stars in common to this VAC and Carretta et al. (2010) are displayed in abundance residuals versus T_{eff} planes in Fig. A2. The top panel compares APOGEE versus Carretta et al. (2010) values for [O/Fe], whereas comparisons of Fe abundances derived using lines due to neutral and once-ionized iron are displayed in the middle and bottom panels, respectively. Non-negligible differences, at the 1σ level, are seen between the two sets of Fe abundances. A mild dependence on metallicity is apparent, with good agreement on the high-metallicity end, and a slight deterioration at [Fe/H] $\lesssim$ −1.0. Overall, we conclude that the agreement between the Fe abundances

of APOGEE and Carretta et al. (2010) is about satisfactory. Regarding oxygen abundances, the mean difference between the two sets is ∼0.1 dex, which is well within the rms scatter, suggesting that the discrepancy between APOGEE and GALAH on the same plane (Fig. A1) is due to systematics in the GALAH data.

We wrap up our verification of APOGEE abundances against the literature by extending our scrutiny to additional elements. Fig. A3 contrast APOGEE abundances with data from a variety of literature sources, originally compiled by Mészáros et al. (2015).[5] Abundances shown are those for C, N, O, Ca, Si, and Al. For all elements, the

---

[5] Sources included are the following: Briley et al. (1997), Carretta et al. (2009), Cavallo & Nagar (2000), Cohen & Meléndez (2005), Ivans et al. (2001), Johnson et al. (2005), Johnson & Pilachowski (2012), Koch & McWilliam (2010), Kraft et al. (1992), Kraft & Ivans (2003), Lai et al. (2011), Lee, Carney & Balachandran (2004), Meléndez & Cohen (2009), Minniti et al. (1996), O'Connell et al. (2011), Otsuki et al. (2006), Ramírez & Cohen (2002, 2003), Roederer & Sneden (2011), Shetrone (1996), Smith, Shetrone & Strader (2007), Sneden et al. (1991, 1992, 1997, 2004), Sneden, Pilachowski & Kraft (2000), Sobeck et al. (2011), Yong, Aoki & Lambert (2006a), and Yong et al. (2006b, 2008).
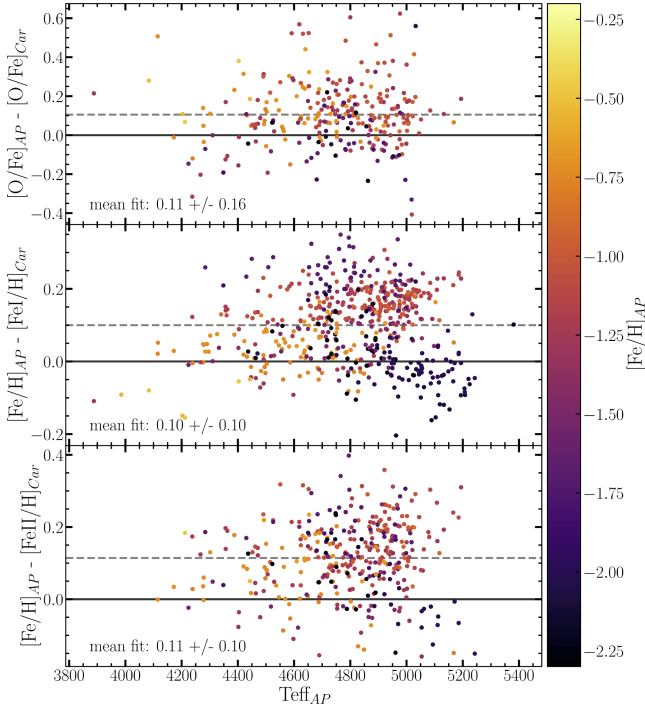
Figure A2. Comparison of APOGEE abundances for O (top panel) and Fe with values obtained by E. Carretta and collaborators (middle panel for abundances obtained from neutral lines, bottom panel for those based on once-ionized iron). Good agreements are achieved for [O/Fe], but for [Fe/H] the mean residuals are off at the 1σ level. There is also evidence for a dependence of residuals on metallicity.
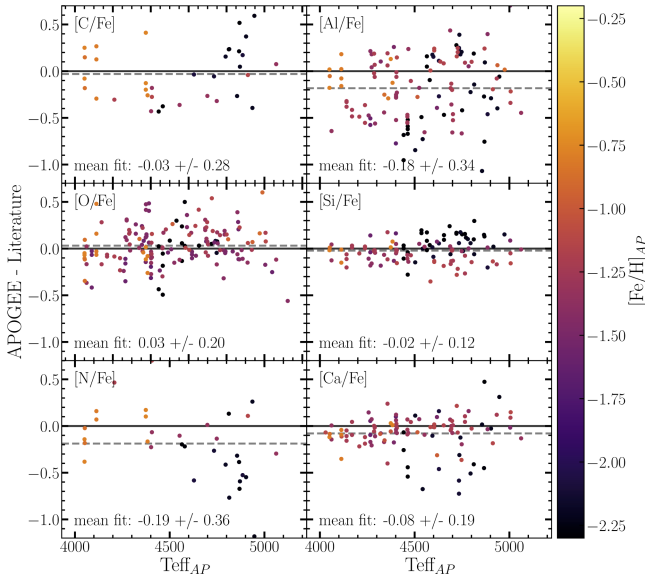
Figure A3. Comparison of APOGEE abundances for other elements with values from other sources in the literature. We find excellent agreement for most elements, and satisfactory agreement for Al and N, with no obvious dependence on metallicity or $T_{\rm eff}$ (except perhaps for N).

mean residuals are consistent with the identity line well within the rms dispersion. For N and Al the scatter is larger, and in the case of the former, there seems to be a dependence on metallicity. This is perhaps not surprising, because APOGEE N abundances rely on CN lines, which become vanishingly weak in giant stars with [Fe/H] $\lesssim$ − 2.0. Outside that regime, an agreement between APOGEE and the literature sources is actually very good.

In conclusion, a comparison between APOGEE chemical compositions and data from GALAH and a compilation of classical abundance analyses from the literature indicates that APOGEE chemistry for Galactic GC members is characterized by excellent precision and very good accuracy.

[1] *Astrophysics Research Institute, Liverpool John Moores University, 146 Brownlow Hill, Liverpool L3 5RF, UK*

[2] *Department of Physics and Astronomy, Texas Christian University, Fort Worth, TX 76129, USA*

[3] *Center for Computational Astrophysics, Flatiron Institute, 162 5th Avenue, New York, NY 10010, USA*

[4] *Instituto de Astrofísica, Facultad de Ciencias Exactas, Universidad Andrés Bello, Fernández Concha 700, Las Condes, Santiago, Chile*

[5] *Vatican Observatory, V-00120 Vatican City State, Italy*

[6] *Departamento de Física, Universidade Federal de Santa Catarina, Trindade 88040-900, Florianópolis, Brazil*

[7] *Instituto de Astrofísica de Canarias, Vía Láctea, s/n, E-38205 La Laguna, Tenerife, Spain*

[8] *Departamento de Astrofísica, Universidad de La Laguna, E-38206 La Laguna, Tenerife, Spain*

[9] *Department of Physics and Astronomy, University of Notre Dame, 225 Nieuwland Science Hall, Notre Dame, IN 46556, USA*

[10] *Department of Astronomy, University of Virginia, Charlottesville, VA 22904, USA*

[11] *Department of Astrophysical Sciences, Princeton University, 4 Ivy Lane, Princeton, NJ 08544, USA*

[12] *The Observatories of the Carnegie Institution for Science, 813 Santa Barbara Street, Pasadena, CA 91101, USA*

[13] *Department of Physics and Astronomy and JINA Center for the Evolution of the Elements, University of Notre Dame, Notre Dame, IN 46556, USA*

[14] *Department of Physics and Astronomy, University of Utah, 115 S 1400 E, Salt Lake City, UT 84112, USA*

[15] *Rutgers, The State University of New Jersey, 136 Frelinghuysen Road, Piscataway, NJ 08854, USA*

[16] *Instituto de Astronomía, Universidad Católica del Norte, Avenida Angamos 0610, Antofagasta, Chile*

[17] *Materials Science and Applied Mathematics, Malmö University, SE-205 06 Malmö, Sweden*

[18] *Centro de Investigación en Astronomía, Universidad Bernardo O'Higgins, Avenida Viel 1497, Santiago, Chile*

[19] *ELTE Eötvös Loránd University, Gothard Astrophysical Observatory, Szent Imre H st 112, 9700 Szombathely, Hungary*

[20] *MTA-ELTE Lendület 'Momentum' Milky Way Research Group, Szent Imre H st 112, 9700 Szombathely, Hungary*

[21] *Center for Astrophysics and Space Astronomy, University of Colorado at Boulder, 389 UCB, Boulder, CO 80309-0389, USA*

This paper has been typeset from a TEX/LATEX file prepared by the author.